JGR Planets

RESEARCH ARTICLE
10.1029/2023JE007887

Key Points:

- This study presents the first analysis of tides from solar occultation observations at Mars
- The dominant wavenumber can change with local time due to the presence of tides with multiple periods at high latitudes
- Diurnal tides in the model diminish with altitude, suggesting the influence of mean winds on vertical propagation

Supporting Information:

Supporting Information may be found in the online version of this article.

Correspondence to:

A. Kumar,
aishsk6@vt.edu

Citation:

Kumar, A., England, S. L., Liu, G., & Thiemann, E. M. B. (2024). Atmospheric tides in the middle and upper atmosphere of Mars at northern high latitudes: A comparison of MAVEN-EUVM and MRO-MCS observations with model results. *Journal of Geophysical Research: Planets*, *129*, e2023JE007887. https://doi.org/10.1029/2023JE007887

Received 6 MAY 2023
Accepted 28 MAR 2024

Atmospheric Tides in the Middle and Upper Atmosphere of Mars at Northern High Latitudes: A Comparison of MAVEN-EUVM and MRO-MCS Observations With Model Results

Aishwarya Kumar[1], Scott L. England[1], Guiping Liu[2], and Edward M. B. Thiemann[3]

[1]Aerospace and Ocean Engineering, Virginia Polytechnic Institute and State University, Blacksburg, VA, USA, [2]ITM Physics Laboratory Heliophysics Science Division, NASA Goddard Space Flight Center, Greenbelt, MD, USA, [3]Laboratory for Atmospheric and Space Physics, University of Colorado Boulder, Boulder, CO, USA

Abstract Much of the variability in the Martian thermosphere can be attributed to vertically propagating atmospheric tides that are known to achieve significant amplitudes in this region. Concurrent observations from different altitudes have been used previously to discern the vertical propagation characteristics of tides but have primarily focused on low latitudes. The spectrum of tides and their vertical evolution are thereby less constrained at high latitudes. Few studies that have focused on high latitudes identified wavenumber-3 structures which were interpreted to originate mainly from the non-migrating tides SE1 and DE2. This paper presents the first analysis of MAVEN-EUVM solar occultation observations to deduce atmospheric tides in the Martian thermosphere. These are compared to tides observed by MRO-MCS in the middle atmosphere for six cases at high northern latitudes. To identify vertical propagation, wave signatures in the middle and upper atmosphere are compared and are found to be dominated by a mix of zonal wavenumbers-2 and -3 in fixed local time. MCS observations show eastward propagating tides dominate, specifically highlighting SE1 near 76 km. Additionally, these observations indicate the presence of stationary planetary waves and terdiurnal tides. Mars Climate Database also indicates the presence of SE1, DE2, DE1, S0, TW1, and T0 tides. A change in the dominant wavenumber component with local time is seen, which is attributed to the presence of all three diurnal, semidiurnal and terdiurnal components at these latitudes. The significant decrease in the diurnal tide amplitude indicates the effect of zonal mean wind on vertical propagation.

Plain Language Summary Atmospheric tides are a kind of wave in the Martian atmosphere that can cause large oscillations in temperature, density, and pressure. Concurrent observations from different altitudes can determine how tides vary as they propagate into the upper atmosphere. Several previous studies have observed wave signatures from a range of heights but focused mainly on equatorial regions. Previous observations from near polar regions revealed strong tidal signatures, producing wave patterns with three peaks in the upper and middle atmosphere, attributed to a mix of waves with one and half a Mars day frequency. Here, using observations from two instruments that simultaneously measure the middle and upper atmosphere of Mars, dominant wave signatures at high latitudes are identified and how they change between these regions are examined. This study presents the first observations of atmospheric tides from new data derived from the extinction of solar radiation in the Martian upper atmosphere. Additionally, the observations are compared to a model, providing insight into how well the model captures the observations. A key finding is that the strongest wave component seen may vary with local time due to the presence of three different waves with one, half, and third of a Mars day frequency.

1. Introduction

Atmospheric tides are now a well-known ubiquitous dynamic feature in observations of the Martian atmosphere. Tides appear as global-scale oscillations in atmospheric variables such as density, pressure, temperature and winds with periods that are harmonics of the Martian solar day. These oscillations are mainly excited due to the cyclic absorption of solar radiation by a rotating planet and its atmosphere (Forbes et al., 2002; Zurek, 1976). Certain tides generated in the lower atmosphere have the characteristics of vertically propagating waves and are capable of carrying energy and momentum from their source region to the upper atmosphere (Conrath, 1976;

Wilson, 2002; Zurek, 1976). The energy carried by them is deposited at higher altitudes via dissipation, contributing to the acceleration of the background atmosphere (Forbes et al., 2002; Jones et al., 2019).

While tides arise mainly as a direct response to solar forcing, they are strongly influenced by the interaction of solar forcing with zonal inhomogeneities in surface topography and thermal properties such as surface albedo, dust loading, and water-ice clouds (Kleinböhl et al., 2013; Withers et al., 2003; Zurek, 1976). Following the mathematical representation and naming convention from Forbes et al. (2002), the atmospheric response to such forcing can be represented by

$$A_{n,s}(z,\theta)\cos\left(n\Omega t + s\lambda - \phi_{n,s}(z,\theta)\right), \tag{1}$$

$$A_{n,s}(z,\theta)\cos\left(n\Omega t_{\mathrm{LT}} + (s-n)\lambda - \phi_{n,s}(z,\theta)\right), \tag{2}$$

where $A_{n,s}$ and $\phi_{n,s}$ are the amplitude and phase of the wave, z and θ are the altitude and latitude, t is universal time (UT), t_{LT} is local time (LT), $\Omega = 2\pi$/sol is the planetary rotation rate, λ is the longitude, n is the period where $n = 1$, 2, 3 refers to diurnal, semidiurnal and terdiurnal or periods of 1 sol, 1/2 sol, and 1/3 sol, respectively; s represents the zonal wavenumber or the number of cycles per 360° longitude. Equation 2 describes the same oscillation in terms of local time, which more conveniently matches the longitude-time dependencies in typical spacecraft observations. It is clear from Equation 2 that the spectrum of tides can be classified broadly into two categories viz., the $s = n$ components called migrating tides, which appear as longitude-independent features in a fixed local time reference frame, and the $s \neq n$ components called "non-migrating tides" that are longitude-dependent and can migrate eastward or westward with phase speeds greater than $\Omega = 2\pi$/sol. An eastward (E) propagating diurnal (D) tide is referred to as DEs, where "s" stands for the zonal wavenumber. If the tide propagates westward (W), it is referred to as DWs, whereas for the eastward or westward propagating semidiurnal (S) tides, "S" replaces the "D" and they are called SEs or SWs, respectively.

While the sun-synchronous migrating tides can cause large perturbations at thermospheric heights (Forbes et al., 2023), they do not produce variation with longitude in a fixed local time reference frame. Non-migrating tides, the subject of the present paper, can cause large amplitude variations with longitude at thermospheric heights (e.g., Keating et al., 1998; Withers et al., 2003). These tides are generated in the lower atmosphere and propagate into the upper atmosphere gaining amplitude as density decreases with height to maintain constant energy density.

It can be seen from Equation 2 that $|s - n|$ is the wavenumber associated with longitudinal variation in a fixed local time reference frame. A few previous studies have successfully delineated values of s and n; however, many of these were focused on identifying migrating tides in the lower atmosphere (Fan, Forget, et al., 2022; Fan, Guerlet, et al., 2022; Guerlet et al., 2023; Kleinböhl et al., 2013). Wu et al. (2015) successfully separated the values of s and n to identify both migrating and nonmigrating tides in the middle atmosphere using MCS observations. While these studies have largely focused on the middle and lower atmospheres, distinguishing between the different tides and minimizing aliasing has been particularly challenging in the upper atmosphere owing to the limited spatio-temporal satellite coverage.

Previous spacecraft observations of Mars' middle and upper atmosphere at fixed local time have shown that the longitudinal structure in the middle and upper atmosphere is generally dominated by a combination of the wavenumber-2 and -3 components (Banfield et al., 2000, 2003; Bougher et al., 2001; England et al., 2016, 2019; Forbes et al., 2020; Keating et al., 1998; Kumar et al., 2022; Liu et al., 2017; Lo et al., 2015; Schneider et al., 2020; Thaller et al., 2020; Withers et al., 2003, 2011). As mentioned above, since many observations do not allow for the separation of s and n, model simulations have been used to identify the most significant non-migrating tides underlying the observed wavenumber-2 and -3 signatures, which are often the DE1, DE2, and SE1 tides (Forbes & Hagan, 2000; Forbes et al., 2002, 2020; Moudden & Forbes, 2008).

Observations that have repeatedly sampled regions closer to the equator at low and mid-latitudes have shown that the wavenumber-2 and -3 components dominate the variability in this region. These signatures have frequently been attributed to the DE1 and DE2 tides, confirming some previous modeling results. Lo et al. (2015) showed the presence of a strong wavenumber-2 signature, which was attributed to the DE1 tide in the MAVEN-IUVS (Mars Atmosphere and Volatile Evolution mission's Imaging Ultraviolet Spectrograph) densities derived from the

CO_2^+UVD emissions at latitudes between 0–30°N. Concurrent observations from MAVEN-IUVS and MAVEN-NGIMS (Neutral Gas and Ion Mass Spectrometer) revealed strong wavenumber-2 signatures at low northern latitudes whose amplitude varied by 50% between 5° and 25°N which is consistent with the behavior of the DE1 tide (England et al., 2016). Schneider et al. (2020) showed the presence of a wavenumber-3 structure near the equator in the NO nightglow brightness, which is interpreted as the DE2 tide by measuring phase change with local time.

At higher latitudes, observations have indicated that the SE1 and S0 tides are the primary contributors to the wave structure. Wavenumber-3 features were identified by Bougher et al. (2001) in the Mars Global Surveyor (MGS) accelerometer data at high northern latitudes between 60 and 65°N, which is attributed to the eastward propagating semidiurnal tide (SE1). Cahoy et al. (2007) also reported the contribution of SE1 tide to the zonal wavenumber-3 structure observed in the MGS electron densities between 60° and 85°N. Altitude-latitude structure of modeled relative density amplitudes sampled at locations of MGS aerobraking phases -I and -II showed that the SE1 amplitudes maximized at high northern latitudes (Angelats i Coll, 2004; Wilson, 2002). The presence of wave-like oscillations with three peaks was identified near ∼68°N in temperature profiles of the Phoenix Mars probe and observations from the Mars Climate Sounder (MCS) instrument aboard the Mars Reconnaissance Orbiter (MRO) spacecraft (Withers & Catling, 2010). The authors suggested that DE2 and SE1 tides are likely responsible for this variability. Recently, England et al. (2019) compared high latitude upper atmospheric observations from MAVEN-IUVS and MAVEN-NGIMS to MRO-MCS observations of the middle atmosphere and identified the presence of a strong wavenumber-3 signature at high southern latitudes, which have been attributed to the SE1 tide. While this study provided much needed insight into tides reaching the upper atmosphere at high latitudes, only two cases at high southern latitudes were analyzed, and no model comparisons were made over a large vertical range.

The aforementioned studies make it evident that the prevailing nonmigrating tides influencing the longitudinal variability in the upper atmosphere vary from the equator toward the poles. Theoretical predictions suggest that the DE1 tide can propagate vertically only at latitudes close to the equator and are confined within ±30°, whereas the semidiurnal components may propagate vertically at higher latitudes (Forbes & Hagan, 2000). Tides that propagate vertically are a well-known mechanism for transferring energy and momentum by interacting with each other as well as the background circulation. General circulation model simulations have shown that upward propagating tides play a crucial contributing role in the winter polar warming features observed in the lower atmosphere and the thermosphere (Bell et al., 2007; Wilson, 1997). Moudden and Forbes (2008) investigated the effects of vertically propagating thermal tides on the zonal mean density, temperature and wind structure in the 90–160 km region using model simulations. By isolating the effects of the non-migrating tides from the migrating tides, the authors show that the changes in all zonal mean fields are dominated by the non-migrating tides owing to their longer vertical wavelengths that allow them to reach higher altitudes before dissipating.

Forbes et al. (2020) performed a comprehensive climatological analysis of tides in the middle atmosphere using MCS temperature measurements and compared it with the Mars Climate Database (MCD v5.3). The findings of this study report good agreement in the amplitudes and structure at 76 km between model tides and MCS climatology. It also demonstrated that MCD captures the thermospheric wavenumber-2 structure exhibited in the MGS density data with comparable amplitudes and phases. While good agreement with MCD is seen near 105–115 km when compared to MGS data, the authors note significant knowledge gaps and differences between model and observations. Examples of these are the poorly constrained distribution of wind in the middle and upper atmosphere, the model's tendency to underestimate the vertical extension of dust and so on. Therefore, a thorough comparison with the model and validation against observed tides at higher altitudes is required to better predict thermospheric variability due to atmospheric tides. Kumar et al. (2022) have inferred vertical propagation of tides at low latitudes by combining observations over a large range of altitudes (from 60 to 165 km) from MAVEN-IUVS, MAVEN-NGIMS and MRO-MCS. Results from this study showed that the observations were dominated by wavenumber-2 and -3 signatures. Further, comparing with the model, the authors found that the likely underlying tides were the diurnal components DE1 and DE2. It was also noted that the model performed much better at lower than higher altitudes.

Here, we focus on characterizing tides and vertical propagation by combining observations at different altitudes and comparing them with model results, similar to Kumar et al. (2022), but with a focus on the high northern latitude region. Data from MAVEN's Extreme Ultraviolet Monitor (EUVM) will provide the observations of the

upper atmosphere, which will be compared with MRO-MCS observations of the middle atmosphere. As stated previously, Forbes et al. (2020) demonstrated that the model compares well with MCS observations in the middle atmosphere and in some cases in the upper atmosphere. Kumar et al. (2022) focused on low latitudes and also showed that the model compared well with MCS observations in the middle atmosphere. However, while the model captured the dominant wavenumber in the upper atmosphere, the amplitudes and phases did not agree with the observations. In this study, observations from high northern latitudes are compared with the Mars Climate Database, highlighting any discrepancies between observations and the model. Such a comparison becomes important to assess the model's ability to bridge the data gap in the region where observations are lacking, especially when inferring the propagation of tides from the middle to upper atmosphere. Furthermore, this comparison aims to help understand how the model's performance at high latitudes compares with that at low latitudes. The following sections are organized as follows: the data utilized in this study and data selection are described in Section 2, the methodology employed to analyze tides and corresponding results for a single case is described in Section 3, followed by discussion and conclusions in Sections 4 and 5, respectively.

2. Data Description and Selection

The data used in this study consists of temperatures derived from the solar occultation measurements made by the EUVM instrument aboard MAVEN and remote sensing measurements made with the MCS instrument on MRO. MCD consists of meteorological fields based on the Mars Planetary Climate Model (Mars PCM) and is used in conjunction with the observational data here, allowing for a comparative analysis between the results produced by the model and observations. This will be done through both sampling MCD at the location of the observations and a spatial-temporal decomposition of the MCD output. With a focus on high latitudes, the upper atmospheric observations are obtained from EUVM temperature profiles that span an altitude range of ∼120–200 km, whereas MCS provides observations of the middle atmosphere from 30 to 80 km. MCD covers this entire range of altitudes and the subsequent results will be referenced against both the middle and upper atmospheric observations.

To combine and compare the different datasets, it is essential to have overlap in the date ranges and latitudes, which decides the ability to estimate wavenumbers, tidal amplitudes and phases, and vertical propagation characteristics. Since this study is focused on understanding the vertical propagation of tides at high latitudes, the data selection (i.e., cases) is driven by EUVM. The following subsections will discuss data from each instrument beginning with EUVM, followed by MCS as well as the model, along with the caveats associated with each dataset in detail.

2.1. EUVM

The Extreme Ultraviolet Monitor instrument consists of filter radiometers that can record solar EUV irradiance in three broad wavelength bands whose ranges span 0.1–7 nm, 17–22 nm, and 117–125 nm, respectively (Eparvier et al., 2015). The EUVM solar occultation measurements have been used to derive thermospheric density measurements using the extinction ratio (ER), which is the ratio of the observed solar intensity at a tangent height to that at the top of the atmosphere. The primary challenge in using solar occultation measurements to retrieve thermospheric densities is accounting for the spatial extent of the solar disk, which is larger than the thermospheric scale heights on Mars. This issue is mitigated by incorporating solar images and reference atmospheres in a forward model of the extinction ratio, which is used to determine the vertical profiles of the column density. The corresponding temperature profiles are then inferred from the derived densities by computing the pressure at each altitude, followed by applying the ideal gas law under the hydrostatic equilibrium assumption. Each retrieved temperature profile has a vertical sampling of less than ∼1 km and the optical depth approaches unity near 130 km. The description above is a very summary of the method used to obtain the vertical temperature profiles and further details can be found in Thiemann et al. (2018).

The data distribution of all available EUVM observations for the years 2015, 2017, and 2018 can be seen in Figure 1a. Due to the nature of solar occultation measurements, the local time is fixed at the terminator near ∼6 a.m. and 6 p.m. for observations close to the equator. Generally, observations that are sampled ∼12 hr apart in local time give an excellent opportunity to implement methods that separate semidiurnal tides from diurnal tides (England et al., 2019; Guzewich et al., 2012; Lee et al., 2009; Steele et al., 2021). However, observations from EUVM at these fixed local times were taken over different months (see Figure 1a); therefore, analysis by implementing such a method is not possible since mixing observations from different months could lead to a bias

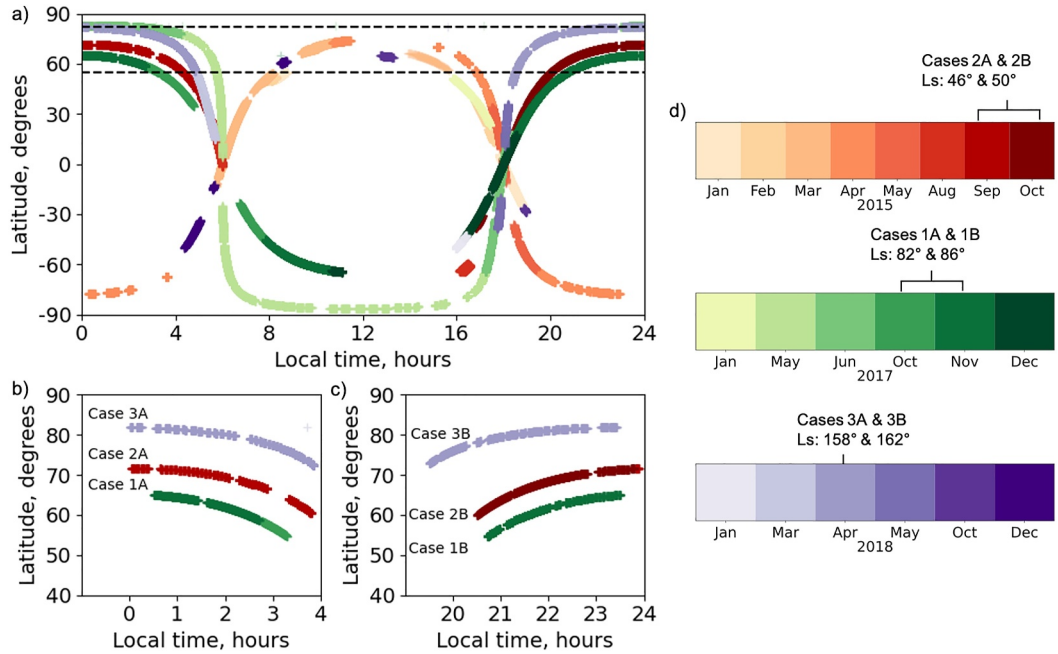

Figure 1. Data from MAVEN-EUVM as functions of local time and latitude. (a) All available data from the years 2015, 2017, and 2018. The colors represent data from different years. (b, c) Shows the selected data from the six cases labeled 1A-1B, 2A-2B, and 3A-3B, respectively. (d) Displays the colors that distinguish different months in Earth year and the cases selected for analysis and their L_s have been marked.

in the results as tides are known to evolve with season (L_s) (Forbes et al., 2020). Therefore, this analysis focuses on fixed high latitudes, where the number of data points is maximized across a small range of local times. To ensure complete longitudinal coverage, observations are limited to latitudes north of 50°. This results in the selection of six cases, as detailed in Table 1, whose latitude-local time coverage is shown in Figures 1b and 1c. Note that for a particular latitude range, each case is divided into two segments such that the observations from these two segments are shifted by 4 hr in local time and less than 5° in L_s. Analyses of these cases are performed separately, and results are compared. These results are expected to be broadly similar given the small separation in L_s between any two segments. Cases are labeled in the order of increasing latitude; for example, the lowest latitudes sampled between 55–65°N provide two cases separated by L_s and local time within this latitude range and are labeled as Case 1A and 1B, respectively.

Densities and temperatures at thermospheric altitudes respond strongly to changes in solar EUV flux (Thiemann et al., 2018). Prior to performing tidal analysis, it is essential to remove the effects of changes in solar EUV from the EUVM data. In order to do this, the irradiance measured by EUVM from the 17–22 nm wavelength band is examined. Irradiance is also measured in the 0.1–7 nm wavelength band, but no irradiances are available from the year 2018 since this channel stopped measuring due to a fault in the instrument. Following England et al. (2022),

Table 1
The Six Selected Cases Based on the EUVM Data Distribution and Their Respective Date Ranges: Mars Years (MY), Solar Longitude (Ls), Latitude, and Local Time Ranges

Cases	Date range	L_s (degrees)	MY	Latitude range (degrees)	Local time range (h)
1A	30 October 2017–6 November 2017	81.9	34	55–65	0.5–3.3
1B	8 November 2017–15 November 2017	85.9	34	55–65	20.7–23.5
2A	20 September 2015–30 September 2015	46	33	60–72	0.1–3.8
2B	30 September 2015–9 October 2015	50	33	60–72	20.5–23.9
3A	9 April 2018–16 April 2018	157.8	34	72–82	0–3.9
3B	17 April 2018–22 April 2018	161.5	34	72–82	19.5–23.5

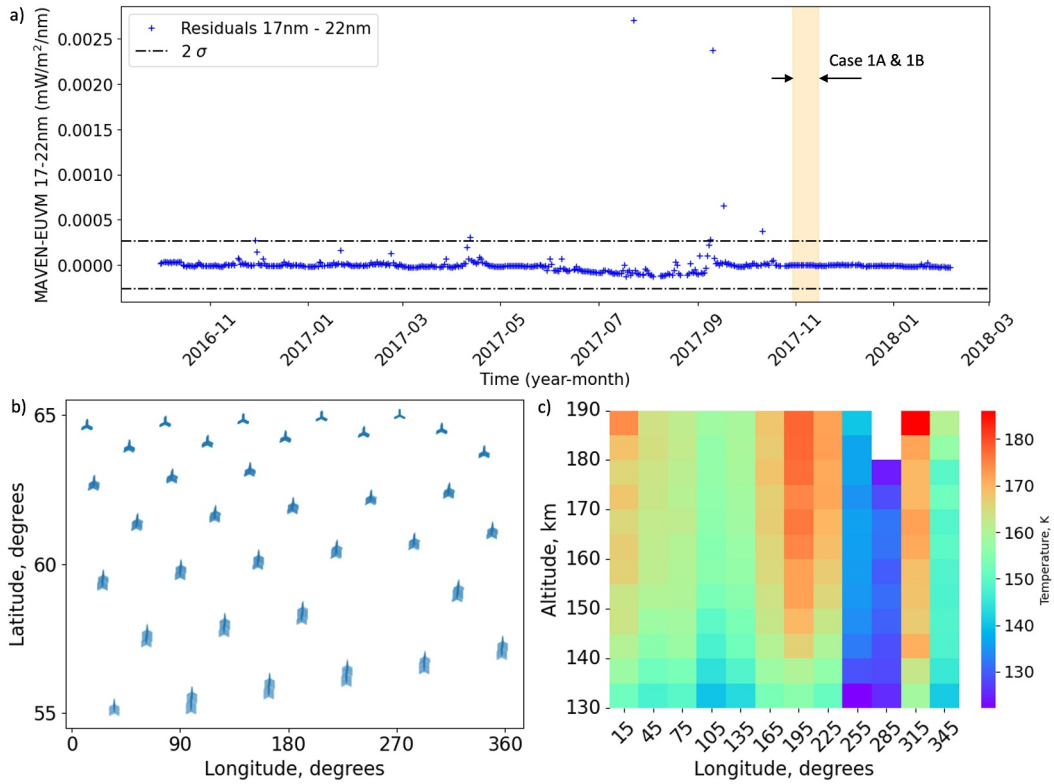

Figure 2. (a) Shows the residuals computed by subtracting the 27-day rolling mean from the daily maximum irradiance obtained from MAVEN EUVM for the year 2017. The dash-dot lines represent the 2σ standard deviation and the vertical black dashed lines mark the region where Case 1A and 1B lie within this time period (b) Shows data distribution of EUVM data for Case 1A as a function of longitude and latitude. (c) Temperature derived from EUVM data for Case 1A shown as a function of altitude and longitude averaged over 55–65° latitude and binned in 5 km altitude and 30° longitude steps. The regions colored white centered at 285° longitude corresponds to a gap due to insufficient data at the two highest altitude bins.

data from days with high solar EUV are removed from the analysis by computing the residuals using the daily maximum solar irradiance and subtracting the 27-day rolling mean from it as shown in Figure 2a. This effectively removes the periodicities associated with the 27-day solar rotation period. Any day that falls outside the 2σ envelope around these residuals is excluded from the analysis. Solar EUV was found to be nearly constant during all time periods considered in this study except October 8 and 10 (in the year 2015), where high solar flux events were recorded; therefore, data from these days are excluded from the analysis.

2.2. MCS

The Mars Climate Sounder instrument is an infrared radiometer onboard the MRO spacecraft, which is in a polar sun-synchronous orbit (McCleese et al., 2007). MCS measures the limb of the atmosphere from the surface to ~80 km with a vertical resolution of 5 km. Vertical profiles of atmospheric temperature used here are obtained from the three channels that measure the 15 μm absorption band of CO_2 (Kleinböhl et al., 2009). The observations taken by MCS are fixed near 3 a.m. and 3 p.m. local time, providing global coverage as the planet rotates under the spacecraft. This study uses MCS data selected for the same time periods (cases) identified by the EUVM dataset at the same latitudes but at different local times. The difference in local times sampled by the two instruments will likely show up as a difference in the phase of the wavenumber signature observed. If tidal phases ($\phi_{n,s}$) are assumed to remain constant with t, then it can be seen from Equation 2 that the phase of the tidal signature ϕ (defined as the longitude of the first peak, which is determined by the terms $n\Omega t_{\mathrm{LT}}$ and $\phi_{n,s}$) changes when sampled at different local times (t_{LT}). Since tidal phases are assumed to remain constant, the phase of the tidal signature ϕ (longitude of first peak) changes when sampled at different local times t_{LT}. The MCS observations are selected to reflect the same date ranges spanned by the EUVM cases, but to ensure sufficient longitudinal coverage, a period of ~one month (~30 sols) of data centered on the EUVM date range is selected. Since tidal

signatures in the Martian atmosphere evolve in timescales that span several weeks to months (Mazarico et al., 2008; Withers et al., 2003), it is reasonable to assume that the identified tidal signatures remain constant over the month of MCS data used in this analysis.

2.3. Mars Climate Database (MCD)

The MCD is a database that provides mean values and statistics of main meteorological variables derived from the Mars Planetary Climate Model (Mars PCM), formerly known as the LMD Mars Global Climate Model (LMD Mars GCM) developed by Laboratoire de Météorologie Dynamique. MCD Version 6.1 (Millour et al., 2017) consists of five broad datasets called "scenarios" that are generated by accounting for the variation in dust and solar EUV conditions in various combinations. In this study, we use the "Mars Years" scenario that pertains to individual Mars Years (MY 24 to MY 34), which best represent the day-to-day EUV forcing conditions and dust loading for a specific Mars year. The MCD outputs are stored on a 5.625° by 3.75° longitude-latitude grid and extend from the surface to ∼300 km. All variables in MCD are stored in 12 Martian months, each spanning 30° of solar longitude (L_s). As noted in Section 1, Forbes et al. (2020) used MCD to characterize tides, and comparison with MCS observations at 76 km showed good agreement at this altitude. Given this agreement between the model and observations in the middle atmosphere, here MCD outputs are compared with observations of tides in the middle and upper atmospheres from MCS and EUVM, respectively.

3. Analysis and Results

Having selected a subset of the data from any of the aforementioned datasets, to quantify the variation in temperature with longitude, a mathematical model in the form of a Fourier series is employed. Given a set of observations, the variation of temperature with longitude in a fixed local time reference frame is modeled by expressing Equation 2 as a sum of sinusoids, as shown below:

$$T = a_0 + \sum_{n=1}^{4} A_n \cos\left(n\lambda - \phi_n\right) \tag{3}$$

where T is the temperature and the dependent variable, λ is the longitude and the independent variable, a_0 is the mean temperature, A_n is the amplitude of the n_{th} harmonic and ϕ_n is the phase of the n_{th} harmonic.

To identify zonal wavenumbers, a least squares estimation method is applied to fit the four-component harmonic model described above to the derived temperature data. This procedure is hereafter referred to as the wavenumber 1–4 fit. Uncertainty in the wavenumber 1–4 fit is quantified by considering the spread in the data, which is essentially estimated by computing the mean squared error between the measured value and the fitted values. We apply this method to analyze the datasets selected from EUVM, MCS, as well as the MCD output. While there is no way of separating the individual contribution of the different tides present by utilizing the EUVM dataset alone, it is possible to infer this information by combining analysis results from the MCS observations and the MCD output. The remainder of this section will discuss the analysis and results of Case 1A as an example and the results from all other cases are provided in the Supporting Information S1.

3.1. EUVM Results

As mentioned in Section 2.1, complete longitudinal coverage is required to characterize tides. The location of the EUVM data as a function of longitude and latitude for Case 1A is shown in Figure 2b and illustrates that this criterion is satisfied. Data selected for Case 1A span latitudes between 55 and 65°N and a local time range of ∼2.8 hr LT (0.5–3.3 hr LT), which is much smaller than the period of the semidiurnal (12 hr) and diurnal (24 hr) tides. Therefore, it is assumed that all the data come from a single local time and will not affect the ability to identify wave signatures, although averaging across different phases of the wave will underestimate the wave amplitudes. At higher altitudes, errors are introduced in the temperature retrievals due to the assumption of a pure CO_2 atmosphere since the contribution of O cannot be neglected at altitudes over 200 km (Thiemann et al., 2018). Furthermore, above 190 km, observations are missing from multiple longitudes; therefore, the altitude range is limited between 130–190 km and these data are binned into 5 km altitude bins and 30° longitude bins. Figure 2c shows the binned temperatures that are then averaged to reveal a clear wave structure that can be identified at multiple altitudes.

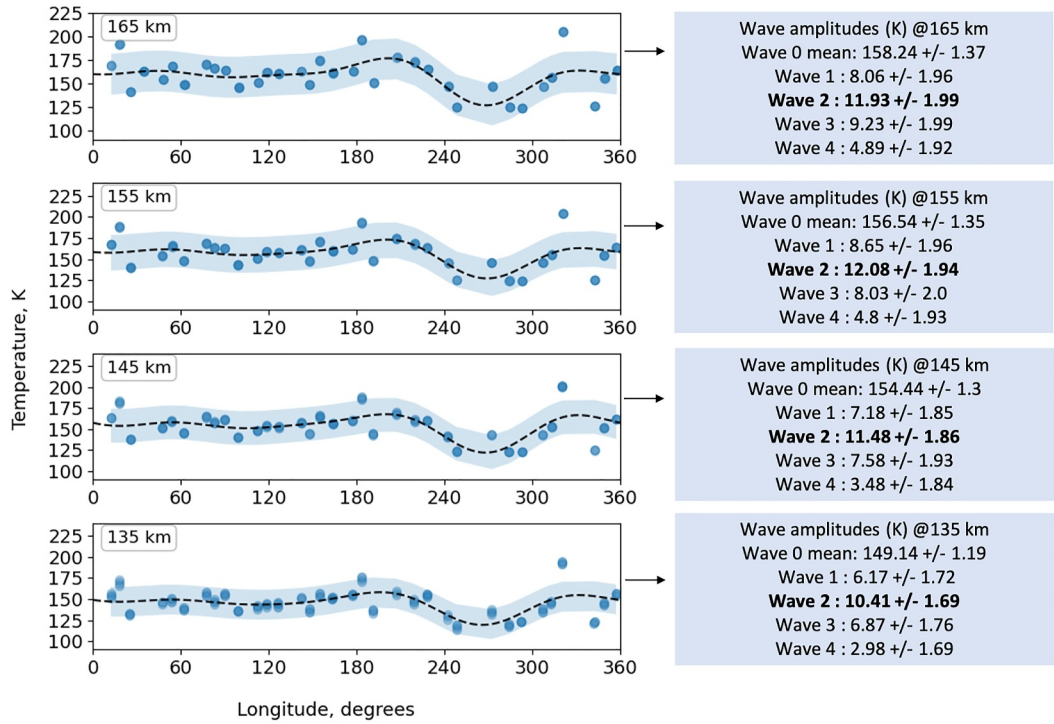

Figure 3. MAVEN-EUVM temperatures as a function of longitude sampled at four altitudes from 135 to 165 km. The blue dots represent the derived temperatures, the black dashed line represents the wavenumber 1–4 fit to the data and the blue shaded region is the $\pm 1\ \sigma$ uncertainty in the fit.

To characterize the wave structure, the wavenumber 1–4 fit is applied to the EUVM derived temperatures in each 5 km bin between 130 and 190 km. Figure 3 shows four sampled altitude bins that capture a clear wave structure with two peaks. The amplitude of the wave appears to change coherently between the altitude bins shown in Figure 3. The derived amplitudes show that the wavenumber-2 component is the strongest and its amplitude increases with altitude until ∼155 km. While the wavenumber-2 signature dominates this spectrum, other waves are also present, notably the wavenumber-1 and -3 components, which also display strong amplitudes.

3.2. MCS Results

MCS temperature profiles are obtained roughly 12 hr apart in local time and are fixed near 3 a.m. and 3 p.m. LT except at high latitudes owing to its orbit. This kind of observation allows for the separation of the diurnal from the semidiurnal tides by examining the summed and differenced temperatures from the two local times (England et al., 2019; Guzewich et al., 2012; Lee et al., 2009). Following the description in Guzewich et al. (2012), a tidal perturbation in the temperatures measured at longitude λ, local solar time t_{LT}, altitude z and latitude θ can be described using Equation 2 as:

$$T'_{n,s}(\lambda, t_{\mathrm{LT}}, z, \theta) = A_{n,s} \cos\left(n\Omega t_{\mathrm{LT}} + (s-n)\lambda - \phi_{n,s}\right) \tag{4}$$

where $A_{n,s}$ and $\phi_{n,s}$ are the amplitude and phase of the oscillation and are functions of z and θ. For the case of sun-synchronous observations from MCS, the local solar time of the ascending and descending portions of the orbit are fixed near 3 a.m. and 3 p.m. local time, and can therefore be written as t_{asc}–$t_{\mathrm{des}} = 12$ which relates a tidal perturbation in the temperatures at t_{asc} given by $T'_{n,s}(\lambda, t_{\mathrm{asc}})$ to that at t_{des} given by $T'_{n,s}(\lambda, t_{\mathrm{des}})$ and can be shown as follows:

$$\begin{aligned} T'_{n,s}(\lambda, t_{\text{asc}}) &= A_{n,s}\cos\left(n\Omega t_{\text{asc}} + (s-n)\lambda - \phi_{n,s}\right) \\ &= A_{n,s}\cos\left(n\Omega(t_{\text{des}}+12) + (s-n)\lambda - \phi_{n,s}\right) \\ &= A_{n,s}\cos\left(n\Omega t_{\text{des}} + n\pi + (s-n)\lambda - \phi_{n,s}\right) \\ &= (-1)^n T'_{n,s}(\lambda, t_{\text{des}}) \end{aligned} \tag{5}$$

Therefore, at a given longitude, the magnitude of the diurnal tide is given by taking half of the difference between two observations taken at two local times 12 hr apart:

$$T'_{\text{diff}} = \frac{1}{2}[T'_{n,s}(\lambda, t_{\text{des}}) - T'_{n,s}(\lambda, t_{\text{asc}})] \tag{6}$$

Summing over all values that can be taken by n and s and substituting Equation 5 in Equation 6, we get:

$$T'_{\text{diff}} = \frac{1}{2}\left[\sum_{n,s} T'_{n,s}(\lambda, t_{\text{des}}) - \sum_{n,s}(-1)^n T'_{n,s}(\lambda, t_{\text{des}})\right] \tag{7}$$

$$T'_{\text{diff}} = \sum_{n_{\text{odd}}}\sum_{s} T'_{n,s}(\lambda, t_{\text{des}}) \tag{8}$$

It is clear from Equation 7 that when n is even or $n = 0$ which represents stationary planetary waves, the RHS of Equation 7 cancels out and becomes zero, therefore leaving only oscillations with odd values of n to be present in T'_{diff}. Similarly, the magnitude of the semidiurnal oscillations can be given by taking half of the sum of two observations taken at two local times 12 hr apart and only oscillations with even values of n will be present in T'_{sum} and is given by:

$$T'_{\text{sum}} = \sum_{n_{\text{even}}}\sum_{s} T'_{n,s}(\lambda, t_{\text{des}}) \tag{9}$$

While this method is powerful in separating the diurnal and semidiurnal components, a few caveats are that it is not possible to distinguish higher order harmonics like the terdiurnal tides from the diurnal tides in the T'_{diff} field. Similarly, it is not possible to distinguish between the stationary planetary waves and semidiurnal components in the T'_{sum} field. Furthermore, observations are ∼12 hr LT apart only at latitudes near the equator and this difference in LT reduces as the spacecraft moves to higher latitudes and passes over the poles. Therefore, for each case analyzed here, the difference in local time between the ascending and descending portions of the orbit varies with the latitude being sampled. For some of the cases, measurements are obtained 11 hr apart, whereas others are 10 hr apart. Therefore, the analysis needs to be interpreted with some caution in the cases that are ∼10 hr apart in LT since the differenced temperature field may include the terdiurnal tide, which has a period of 8 hr of LT. The presence of the terdiurnal tide will be taken into account using a new technique outlined later in this section, along with a spectral decomposition of the full tidal spectrum from the model, which will be discussed in Sections 3.3 and 4, respectively.

MCS data are available for the same latitude range as the EUVM data from 55 to 65°N for Case 1A. The temperature profiles are selected from two local time ranges which span ∼1h each and are centered at 3.2 and 14.3 hr LT. These data are then binned onto a 4 km by 30° altitude-longitude grid and are averaged. The diurnal components are identified by examining the difference between the ascending and descending portions of the orbit, whereas the semidiurnal components are identified by examining the sum of these data. A wavenumber 1–4 fit is performed at each 4 km altitude step to the summed and differenced temperature fields. The phase of each individual wavenumber component is defined as the longitude of the first peak or maxima east of 0°.

As shown in Figure 4, the reconstruction of the wavenumber–2 and–3 components have the highest amplitudes in both the LT summed and differenced temperature fields above 60 km. On comparing the wave amplitudes at 76 km shown in Table 2, we see that the wavenumber–3 component in the LT sum has the biggest amplitude,

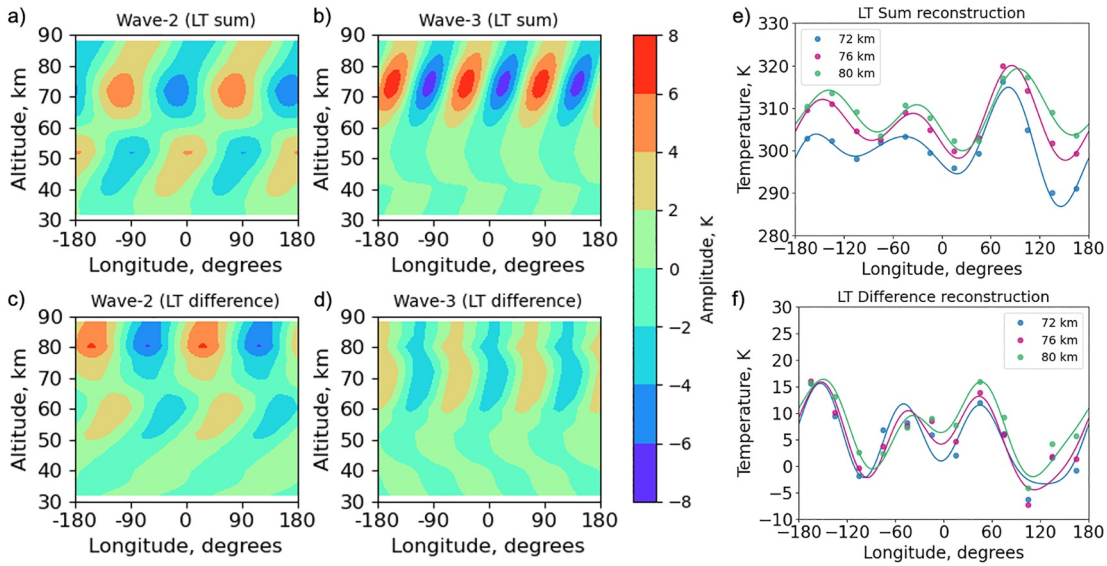

Figure 4. Reconstruction of the sum and difference of the wavenumber-2 and -3 components of the fits to the MRO-MCS temperature data for Case 1A. Separate wavenumber 1–4 fits are performed on the temperature data at each 4-km altitude step. Panels (a) and (b) show the temperature "sum" of the ascending and descending nodes, whereas panels (c, d) show the "difference" between them. Panel (e) shows the reconstruction using all fitted parameters for the LT summed temperatures at 72, 76, and 80 km (f) same as panel (e) for LT differenced temperatures.

followed closely by the wavenumber–2. From Figure 4, we also see that the observed changes in both amplitude and phase seem to be coherent from one altitude bin to the next, especially at altitudes upward of 60 km. Figure 4b shows that the phase (longitude of maxima) has an eastward tilt with height between 70 and 90 km in the reconstructed local time summed temperatures. The eastward progression in height alone is not sufficient to delineate the possible tides responsible for the wavenumber-3 structure in fixed LT, which could be the SE1 or SW5 tide or the stationary planetary wave SPW3 ($s = 3$, $n = 0$). Moreover, since the local times of the ascending and descending nodes are less than ∼12 hr apart, a contribution from the T0 tide may also be present.

While there are clear advantages to the LT sum and difference method described above, there are a few caveats associated with it, the most important of which is the aliasing of the observations related to sampling from a sun-synchronous orbit with t_{LT} = constant. For example, observations limited to just two local times cause stationary planetary waves to be aliased with the semidiurnal tides and it is therefore not possible to distinguish between them. In addition, as seen from Equation 2, it is not possible to distinguish between wave components that

Table 2
Amplitudes Derived From the Wavenumber 1–4 Fit to the EUVM and MCS Data for Case 1A Compared With MCD Amplitudes for the Same Sampling as the Observations

Case 1A L_s 81.9° MY 34	EUVM T (K) @ 155 km	MCD-EUVM T (K) @155 km	MCS T (K) @76 km		MCD-MCS T (K) @76 km	
			153.3260 ± 0.4275		152.16	
Mean	156.5 ± 1.3	167.56	LT sum	LT difference	LT sum	LT difference
Wave 1	8.6 ± 2.9	0.62	0.97 ± 0.62	0.92 ± 1.58	0.15	0.61
Wave 2	**12.1 ± 1.9**	**3.44**	2.24 ± 0.59	1.72 ± 1.52	1.06	2.24
Wave 3	8.0 ± 2.0	1.35	**3.48 ± 0.39**	1.43 ± 1.47	**2.72**	**3.09**
Wave4	4.8 ± 1.9	0.0	0.32 ± 0.59	**1.99 ± 1.70**	0.33	0.65

Note. Amplitudes are computed from the average over 155–165 km altitude for EUVM and are given as absolute temperature amplitudes. For MCS, the amplitudes from the fitted local sum and difference are reported at 76 km. Uncertainties are reported only for the observations. The bold values indicate the dominant wavenumber at for each observation and model result.

represent the same value of ($|s - n|$) using data at only one altitude. While MCS observations are typically measured "in-track", which is fixed near 3 a.m. and 3 p.m. LT, additional local times have also been measured in modified observation campaigns, giving "cross-track" and "off-track" measurements (Kleinböhl et al., 2013). While this strategy provides a total of six local time bins near the equator to about 60°N and S, the local-time sampling is still sparse since the observed local times are clustered near the "in-track" observations. Kleinböhl et al. (2013) used MCS observations at these additional local times to study the migrating semidiurnal tide. The authors showed that the semidiurnal tide had a dominant response throughout the Martian year but did not investigate the non-migrating tides. Wu et al. (2015) investigated both migrating and nonmigrating tides using MCS observations at additional local times and reported the presence of DW3, DW2 and SW1 tides for the first time in the middle atmosphere. However, the authors did not investigate the presence of stationary planetary waves or terdiurnal tides. Here, similar to Wu et al. (2015), MCS data at additional local times are used to derive the amplitudes of the nonmigrating tides and these are compared with the results obtained by the LT summed and differenced temperature fields. This is done by fitting the tides inferred from the LT summed and differenced temperatures to all available data in the longitude–local-time space. The amplitudes obtained for the tides are then compared to the results obtained from the LT sum-difference method. A controlled experiment in Appendix A shows the application of this method to idealized tides that are sampled at MCS local times, which yields good results. Additionally, tidal amplitudes obtained from a control case that samples MCD at the locations of all available MCS observations (rather than just two local times) are also compared with those obtained from an FFT of the full diurnal cycle from MCD for Case 1A to establish a degree of uncertainty on the resultant fit. It is important to note that this method requires adequate local time sampling to separate the tides of interest. In Cases 3A and 3B, however, the local time samples are too sparse to effectively distinguish between these tides, rendering the method unsuitable for these cases.

The method described above is applied to the MCS data by fitting tides inferred from the local time sum and difference temperature fields. For case 1A, these tides are the eastward propagating SE1, DE1, and DE2, the zonally symmetric tides S0 and T0, along with the westward propagating tides that give rise to the same $|s - n|$ zonal wavenumber, which are SW4, SW5, DW3, DW4, and TW1. The stationary planetary wavenumber- 2 and -3 (SPW2 ($s = 2, n = 0$) and SPW3 ($s = 3, n = 0$)) are also fitted to this data since these can be aliased into the LT summed temperature field and cannot be separated out. The MCS temperature profiles at the available local times are binned and averaged in 0.5 hr LT bins and 30° longitude bins. All the selected tides are fitted together to the data between 30–80 km in 4 km altitude steps. The amplitudes of all the fitted eastward and westward propagating tides as a function of altitude are shown separately in Figures 5a and 5b, respectively. The wave amplitudes of the eastward propagating components are clearly larger than their westward counterparts, which is within the expectation and confirms results from previous studies (Forbes et al., 2002; Wilson, 2000). SE1 dominates this tidal spectrum above 72 km, followed closely by DE2 whose amplitude is bigger than the wavenumber-3 amplitude in the LT differenced fields, as shown in Table 2. Similarly, S0, which contributes to the wavenumber-2 structure, is found to have a lower amplitude than indicated in the LT summed fields. Both SPW2 and S0 give rise to the same $|s - n| = 2$ zonal wavenumber structure in a fixed local time reference frame. Figure 5a shows that SPW2 could be present in the tidal field with non-negligible amplitudes and becomes comparable to S0 near 76 km. The terdiurnal tide T0 is shown to be negligible, and the amplitude of the TW1 tide is very small up to 72 km. However, between 76 and 90 km, the amplitude of TW1 becomes comparable to S0 but remains smaller than the dominant tides. It is important to note that MCS observations are less reliable over 76 km, as demonstrated in Figure A3, where the uncertainties on the wave amplitudes increase above this altitude. In general, the method seems to confirm the dominance of the SE1 tide near 76 km, but the incomplete coverage in local time could be underestimating its amplitude while also leading to an overestimation of SPW2, which can be seen in the MCD based analysis in Figure A3. The presence of DE2 with significant amplitude in Figure 5a, but not in the LT differenced fields, is likely due to the presence of terdiurnal tides which cannot be separated from the diurnal components. Given the available local times, the tidal amplitudes derived from this method are most reliable for the four or five biggest tides present. In order to fully distinguish between the minor components, additional local time coverage will be required.

3.3. MCD Results

MCD outputs are analyzed by sampling the model derived temperatures at the same latitudes, local time ranges, and altitudes as the EUVM and MCS datasets. For Case 1A, MCD is sampled at $L_s = 82°$ which represents the

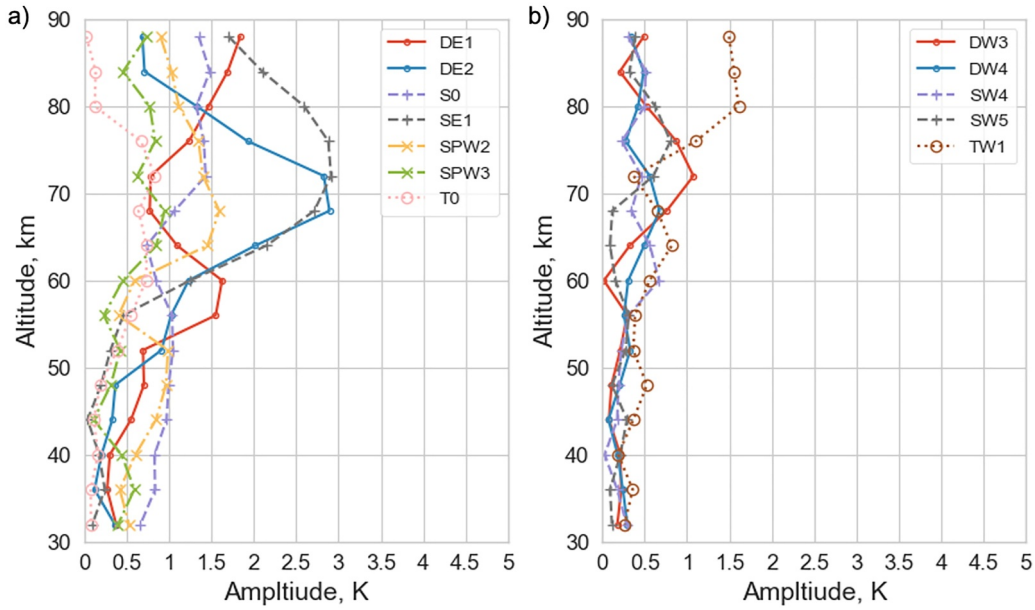

Figure 5. The amplitudes of the eastward and westward propagating components and the stationary planetary waves as a function of altitude derived from wave-fits to the MCS data from all available local times for Case 1A. The fits are performed separately at each altitude bin; the dotted lines indicate the terdiurnal components, the dashed lines indicate semidiurnal components, the solid lines indicate diurnal components and the dash-dot lines indicate stationary planetary waves. (a) shows the amplitudes of the eastward propagating semidiurnal tides SE1, the diurnal tides DE1 & DE2, the zonally symmetric tides S0 and T0 and the stationary planetary waves SPW 2 & SPW3. (b) same as panel (a) but for SW4, SW5, DW3, DW4, and TW1.

midpoint of the date range. To best emulate the observations from Case 1A, the model is sampled at three latitudes, 55, 60 and 65°N, respectively. The longitudinal resolution of the samples is fixed to the same grid size as that of the model itself which is 5.625°, whereas the local times are sampled at 0.5 hr steps.

To capture EUVM observations, the MCD output was further constrained by sampling local times between 0.5–3.3 hr to match the observations. The temperatures obtained from the MCD are then analyzed using the same techniques discussed in Section 3.1. MCD is sampled at the same four altitudes as the EUVM observations and is shown in Figure 6e, where a clear wave signature with two peaks can be seen at all altitudes. The altitude of 155 km is chosen as the reference for comparison across all cases due to the absence of EUVM temperature data below 145 km for Cases 3A and 3B. From the wave amplitudes in Table 2, at 155 km, we see that the wavenumber-2 component is dominant, which is in good agreement with the observations. It is important to note that although there is agreement in dominant wavenumber, MCD derived wave amplitudes are significantly underestimated and the mean temperatures do not agree very well.

In addition to comparing MCD sampled at the exact location as the observations, a spectral decomposition is also performed using the full MCD longitude-local time sampling at the same latitudes and altitudes as EUVM. The Fourier decomposition of the MCD derived temperature field for Case 1A at 145 and 155 km is shown in Figures 6c and 6d. It is evident that the semidiurnal component SE1 is dominant at both altitudes. At 145 km, the S0 tide is observed as the second strongest. The same components are also present at 155 km, with SE1 still being dominant.

To best replicate the conditions of the MCS observations, in addition to sampling MCD at the same latitudes as Case 1A, the same altitude of 76 km is chosen, following which the MCD derived temperatures are averaged and differenced using ∼1 hr LT samples that are separated in local time by ∼11 hr as described in Section 3.2. The MCD derived wave amplitudes in Table 2 show that the wavenumber-3 component is strongest, agreeing well with observations. However, the contribution from the diurnal component is slightly greater than that from the semidiurnal component, which is in contrast with the observations that see a clear dominance of the semidiurnal component. The mean temperatures from the MCD seem to be in good agreement with the observations at 76 km.

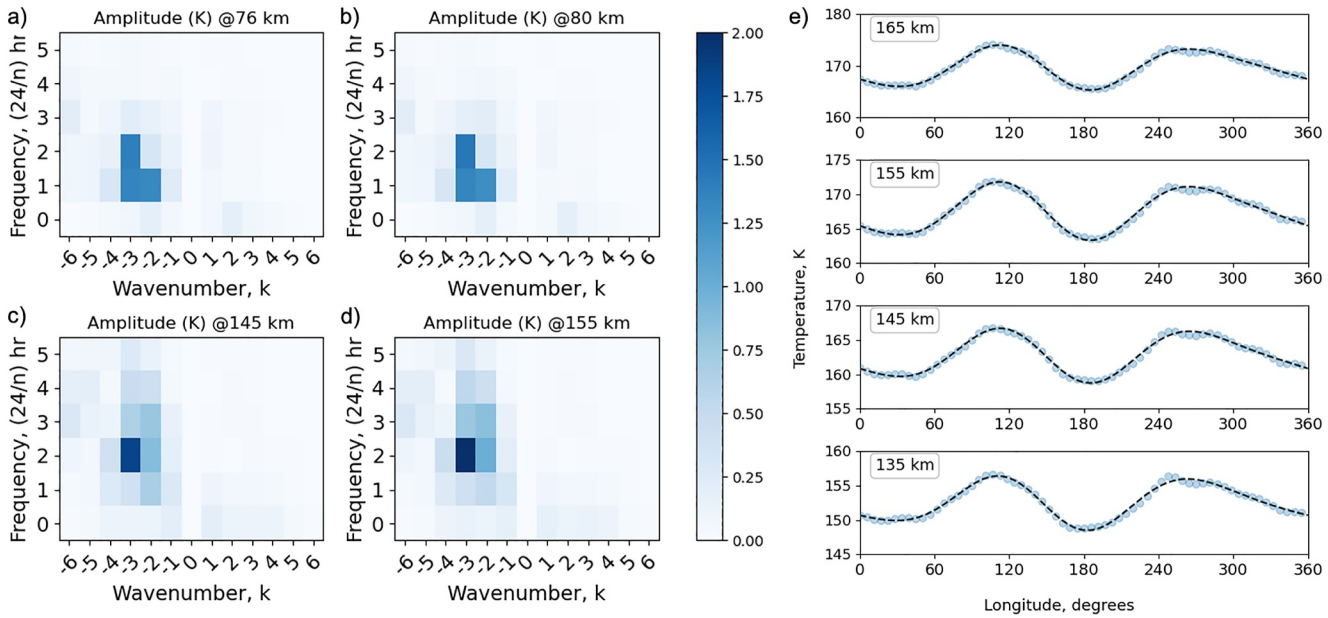

Figure 6. Panels (a–d) show the spectral decomposition of the full MCD temperature distribution for Case 1A. Panels (a, b) show Fourier components at MCS altitudes of 76 and 80 km, whereas panels (c, d) show Fourier components at EUVM altitudes of 145 and 155 km. The most prominent tides in these panels are the SE1 ($n = 2$, $k = -3$), DE2 ($n = 1$, $k = -3$), DE1 ($n = 1$, $k = -2$), S0 ($n = 2$, $k = -2$) and TW1 ($n = 3$, $k = -2$). Panel (e) shows the MCD output sampled at EUVM locations as a function of longitude sampled at four distinct altitudes from 135 to 165 km (similar to fits to EUVM observations in Figure 3). The blue dots represent the model derived temperatures and the black dashed line represents the wavenumber 1–4 fit to the data.

The spectral decomposition for Case 1A at MCS altitudes is shown in Figures 6a and 6b. At both sampled altitudes 76 and 80 km, the semidiurnal component SE1 is strongest, but the diurnal DE1 and DE2 have an almost equally strong presence. Additionally, comparing the Fourier components at all altitudes shows that the amplitude of SE1 increases with altitude.

Changes in amplitude and phase with altitude are shown in Figure 7 for (a) the wavenumber-2 and -3 LT summed and differenced MCS temperatures, (b) the MCD derived wavenumber-2 and -3 LT summed and differenced temperatures, and (c) the individual tides S0, SE1, DE1 and DE2 obtained from fitting to all available LTs as described in Section 3.2. Figures 7a–7d show the phase as a function of altitude and an eastward tilt is seen in the LT summed wavenumber-2 and -3 temperature fields, which is less evident in the LT differenced fields, especially at the higher altitudes. While model phases also resemble this eastward tilt in both the LT summed and differenced fields, the phases seem to be offset from the observations.

Figures 7e and 7h show the amplitude as a function of altitude, where the derived wave amplitude increases with altitude above 60 km in the LT sum field and maximizes near 76 km. Figure 5a indicates that the eastward propagating SE1 and S0 are the primary contributors to the wavenumber-2 and -3 structures in the LT summed fields, whereas DE1 and DE2 are the main contributors to these wave signatures in the LT differenced fields. In addition to the most likely tides listed above, MCD amplitudes of the wavenumbers −2 and −3 components reconstructed from the model derived LT sum and difference temperatures are computed. First, we compare the MCS LT summed and differenced amplitudes to the MCD amplitudes and see that the best agreement is for the LT summed wavenumber-3 component, which is also the dominant component. The amplitudes of the LT summed wavenumber −2 component are underestimated by the model. Model derived amplitudes for the LT differenced wavenumber −2 component agree within the fitted uncertainties at most altitudes, whereas the amplitudes of the LT-differenced wavenumber-3 components are overestimated. Second, we compare the amplitudes of each individual tide obtained by fitting to all available MCS data, which are assumed to be the underlying contributor to the observed longitudinal wave structure. The amplitude of the tide most likely to contribute to a particular wavenumber component is compared to the summed and differenced fields, as seen in Figures 7e–7h. The amplitude of the SE1 tide is remarkably similar to the wavenumber-3 component (in the LT sum). This coherence of the amplitudes with altitude from both methods provides additional confidence in the presence of the SE1 tide.

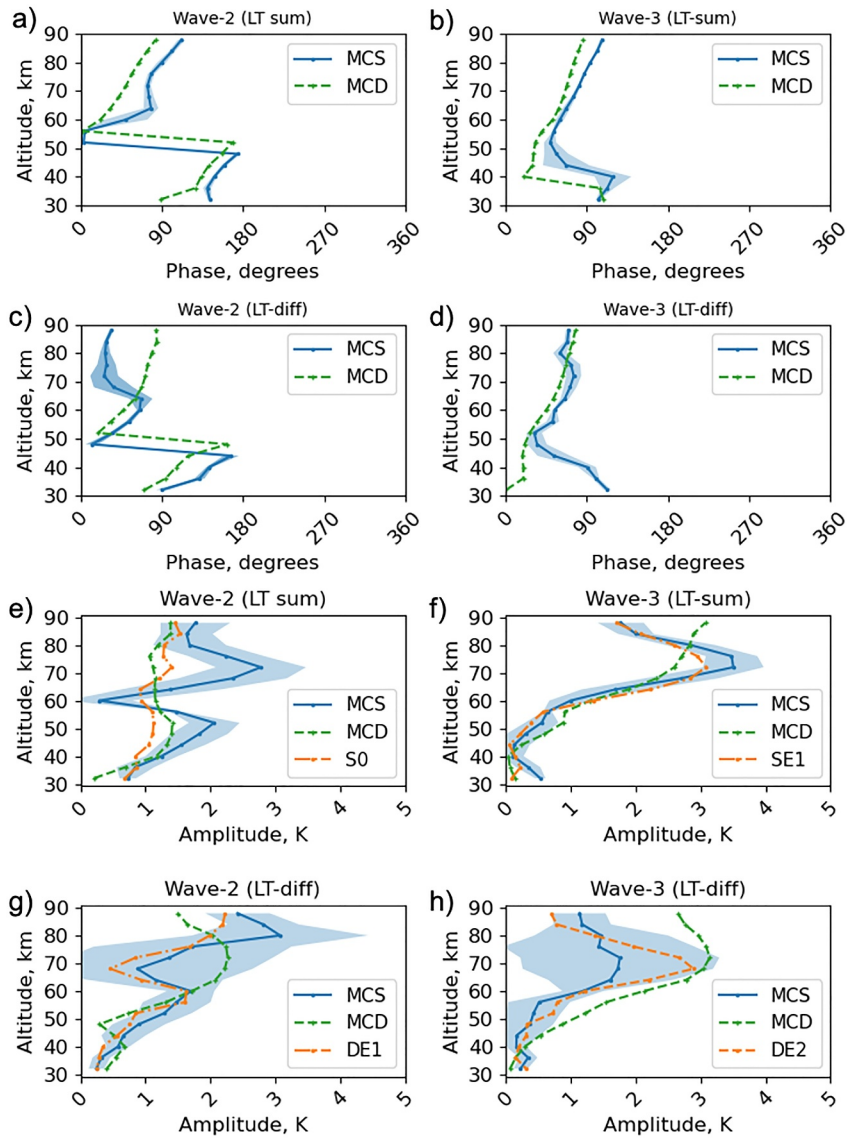

Figure 7. Comparing the wave phases (top four panels) and amplitudes (bottom four panels) derived from the MCS LT summed and differenced temperatures, MCD, and the fit to MCS temperatures from all available local times for Case 1A. Panels (a, b) show the phase as a function of altitude derived for wave-2 and -3 LT summed temperatures compared with MCD. Panels (c, d) same as panels (a, b) but for the LT differenced temperatures compared with MCD. Panels (e, f) compare the derived amplitudes as a function of altitude of the wave-2 and -3 LT summed temperatures with both MCD and the S0 and SE1 amplitudes derived from fitting to all available LTs. Panels (g, h) are the same as panels (e, f) but for the LT differenced temperatures compared with both MCS and the DE1 and DE2 amplitudes (derived from fitting to all available LTs). The blue shaded region is the $\pm 1\ \sigma$ uncertainty in the fit to the MCS data.

4. Discussion

This section begins with a detailed discussion of the results from Case 1A, followed by a summary of the results for the remaining cases and a comparison to observations and model results at low latitudes.

4.1. Observations and Model Results for Case 1A

From Table 2, it is seen that the wavenumber −2 component is strongest in observations of the upper atmosphere. Assuming that this wavenumber-2 structure arises due to vertically propagating tides, the wave amplitude seems to increase with altitude by a factor of 5 or 6 between 76 and 155 km, which is consistent with vertical propagation

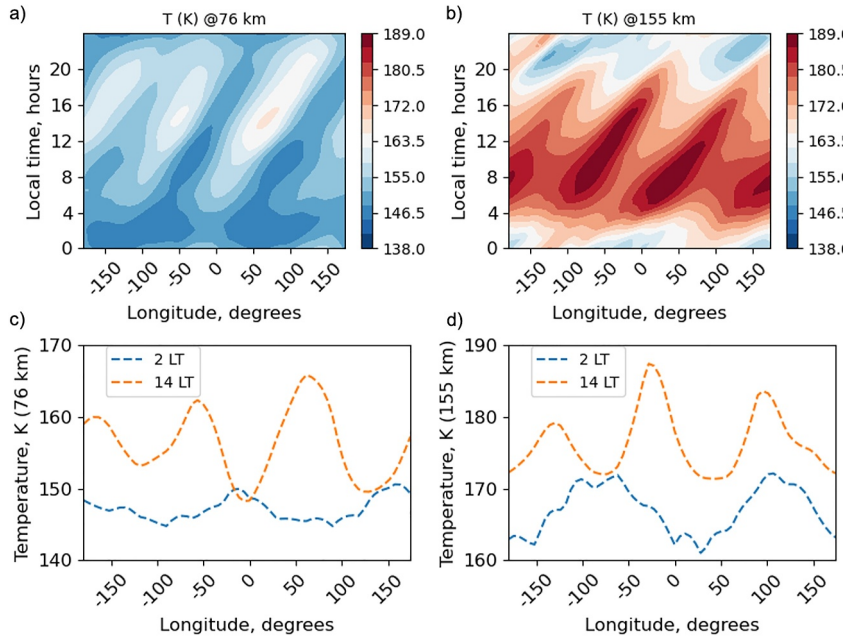

Figure 8. Longitude-local time structures of MCD temperatures sampled at the same latitudes and L_s as Case 1A (55–65° N and L_s 82°). The temperatures are binned and averaged in a longitude–local-time grid with a resolution of 30° by 0.5 hr (a) represents the full diurnal cycle at the altitude of the MCS observations at 76 km. (b) same as panel (a) but at the altitude of the EUVM observations at 155 km. (c) Temperature as a function of longitude sampled at 2 and 14 hr LT from panel (a) at 76 km (d) Same as panel (c) but for panel (d) at 155 km.

assuming density decreases with altitude. While the dominant wavenumber seems to change between 76 and 155 km from wavenumber-3 to wavenumber-2 component, at 76 km both components are present with comparable amplitudes. The inference of vertical propagation must be done with caution since there are no observations between 90 and 130 km. Furthermore, it is important to note that while change in dominant wavenumber from the middle to the upper atmosphere could be the result of differences in the upward propagation of one tide versus another, one other viable mechanism is in situ wave generation in the upper atmosphere (Forbes et al., 2020).

MCD sampled at the same location (altitude, latitude, local time, L_s) as both the MCS and EUVM observations agree upon the dominant wavenumber component but not on the derived wave amplitudes. While the wave amplitudes seem to grow with altitude in both the observations and the MCD (see Table 2 and Figure 6), the estimated growth in wave amplitude is underestimated in the MCD output. Note that the EUVM observations have larger uncertainties at the lower end of the altitude range due to the use of single scale-height reference atmosphere in the retrieval and may therefore inflate the margin of uncertainties in the wave amplitudes computed (Thiemann et al., 2018).

4.2. Dominant Wavenumber Varying With Local Time

When comparing Cases 1A and 1B, the dominant wavenumber is expected to remain consistent. This is due to the mere 4° L_s difference between the two cases and the fact that a local time shift would result in a phase change, not a change in dominant wavenumber (England et al., 2016; Withers et al., 2011). Observations from the upper atmosphere indicate that the wavenumber −2 component is strongest in both these cases, aligning with the expectation. While MCD results also identify wavenumber-2 as strongest in both cases, an equally strong wavenumber −3 is seen in Case 1B (Table S1 in Supporting Information S1). Furthermore, observations from Cases 2A and 2B reveal a change in the dominant wavenumber with local time from the wavenumber −3 to wavenumber −1 component as seen in Tables S2 and S3. Similarly, in Cases 3A and 3B, Tables S4 and S5 show that the dominant wavenumber changes from wavenumber-3 to the −2 component. To understand this change in dominant wavenumber with local time, the full diurnal cycle of MCD (see Figure 8) is examined alongside the Fourier decomposition shown in Figure 6. From Figures 8c and 8d, a change in wave structure

with local time is seen between 2 a.m. and 2 p.m. LT, where the model temperatures at the former LT are characterized by a wave signature consisting of two peaks and the latter with three peaks. The Fourier decomposition shown in Figures 6c and 6d reveals the presence of diurnal, semidiurnal and terdiurnal non-migrating tides in the upper atmosphere that all produce wavenumber-2 structures, in addition to the dominant SE1 tide which gives rise to the wavenumber-3 structure. While the amplitudes of the wavenumber-2 producing tides may individually be smaller than the SE1 tide, these tides may interfere at certain local times, giving rise to a dominant wavenumber-2 component rather than the wavenumber-3 component produced by the SE1 tide, which dominates at other local times. This implies a potentially important limitation of using data from a single local time to infer the dominant tides, which has been commonly employed by previous studies.

4.3. Diurnal and Semidiurnal Tides at High Latitudes

In the middle atmosphere, analysis of MCS observations suggests that the dominant wavenumber arises in the LT sum, which is indicative of a contribution from semidiurnal tides although stationary planetary waves may also be present (see Figure 4b and Table 2). Conversely, analysis of MCD suggests that the diurnal component is dominant, although the semidiurnal component is nearly as strong (see Table 2). Analysis of MCS data from all local times shown in Figure 5 suggests the presence of both semidiurnal and diurnal tides, with the eastward propagating semidiurnal tide SE1 dominant at 76 km. The MCD FFT at this altitude shows that both SE1 and DE2 tides are dominant and have comparable amplitudes, followed closely by DE1 (Figures 6a and 6b). This is consistent with the results obtained by fitting to MCS observations from all available local times, but at 72 km and above SE1 begins to dominate. Focusing on the upper atmosphere, MCD FFT suggests that the semidiurnal tide SE1 is consistently the strongest, but diurnal and terdiurnal components are also present with relatively smaller amplitudes.

4.4. Stationary Planetary Waves

Figure 5 also indicates the presence of both SPW2 and SPW3, although with relatively small amplitudes, assuming the fit accurately captures the underlying variability. In contrast with these observations, the MCD FFT shows that both SPW2 and SPW3, while present, have negligible amplitudes for Case 1A, which can be seen in Figure A3.

4.5. Dissipation of the Diurnal Tide

The MCD FFT shows that while the eastward propagating semidiurnal tide SE1 grows in amplitude with increasing altitude, the diurnal components tides DE1 and DE2 diminish significantly (see Figure 6). The zonal mean zonal wind field is an important parameter in determining the vertical propagation characteristics of tides. If favorable background wind conditions exist, the eastward propagating diurnal tide may propagate to the upper atmosphere at high latitudes (Ekanayake et al., 1997; Forbes et al., 2001). Particularly for the eastward propagating tides, propagation is favored in the westward wind regime where doppler shifting to higher frequencies leads to an increase in vertical wavelengths and therefore, less susceptibility to dissipation (Forbes et al., 2020). The noted decrease in the amplitude of the diurnal tides here suggests that these tides do not propagate to the upper atmosphere. Further, examining Figure 7d from Forbes et al. (2020), which represents the zonal mean zonal wind in MCD for L_s 60–90°, it is seen that at 60°N and between 80–120 km, the MCD wind strength is not sufficient to favor vertical propagation of the diurnal tide even though the winds are westward.

4.6. Terdiurnal Tides at High Latitudes

Middle atmospheric observations and MCD results show that TW1 could be present with very small amplitude and that it grows with an altitude upward of 76 km. The MCD FFT in Figure 6 not only reveals that the TW1 tide gains amplitude with altitude above 76 km but also highlights its presence in the upper atmosphere, as seen in panels (c) and (d). While upward propagation is one mechanism for TW1 to reach thermospheric altitudes, it may also be generated via nonlinear interactions between two primary waves. Such an interaction generates two secondary waves, one corresponding to the sum of the frequency and wavenumber of the interacting primary waves and the other corresponding to the difference between them (Teitelbaum & Vial, 1991). TW1 could arise

from nonlinear interaction between DW1 and S0 or TW3 and SPW2 (Forbes et al., 2021). Forbes et al. (2021) analyzed MCD and identified TW1 as a contributor to the wave-2 structure observed in TGO densities during the polar phase of the orbit. The authors also identified the presence of DW1 and S0 in MCD, indicating that TW1 was generated via interaction between these two tides. While DW1 is not identified in this analysis, the MCD FFT in the upper atmosphere, as shown in Figures 6c and 6d, indicates the presence of both TW1 and S0, which is consistent with the interpretation in Forbes et al. (2021). On the other hand, fit to MCS observations at all available local times in Figure 5 suggests that both S0 and SPW2 are present with comparable amplitudes. This is perhaps in contrast with MCD, indicating that the interaction between SPW2 and TW3 could be the origin of TW1. Recently, Forbes et al. (2023) analyzed NGIMS data and revealed that TW3 is present with amplitudes that are $\sim\leq$10% near 180 km.

4.7. Summary of Results From All Cases

In the upper atmosphere, near 60°N observations from Cases 1A and 1B indicate a dominant wavenumber-2 component although other waves may be present. Near 66°N, Case 2A shows a strong wavenumber-3 component, whereas Case 2B indicates a strong wavenumber-1 component, but wavenumber −3 is the second strongest. And lastly, near 77°N, Case 3A shows a strong wavenumber–3 component, whereas Case 3B shows a strong wavenumber −2 component. While the dominant wavenumber seems to change with latitude based on the cases analyzed here, it is hard to tie a specific latitude to a specific wavenumber since the strongest wave seems to vary with local time in the upper atmosphere. Moreover, since each of the case pairs are sampled at different seasons, it is hard to separate seasonal from latitudinal variation.

Unlike the upper atmosphere, change in local time does not seem to affect the middle atmosphere, where observations indicate that wavenumber-3 component is the strongest for Cases 1A, 1B, 3A, and 3B and the wavenumber −2 component is strongest in Cases 2A and 2B.

MCS observations from all available LTs for Case 1B (Figure S6 in Supporting Information S1), while largely similar to Case 1A, indicate a relatively bigger presence of SPW2 above 60 km and a smaller presence of the DE1 tide. For Cases 2A and 2B (Figures S7 and S8 in Supporting Information S1), SE1 and S0 tides dominate above 60 km, but SPW2 is significant, particularly at altitudes below 60 km. This is consistent with previous results from Guzewich et al. (2012), which identified that the SPW2 dominates all latitudes and altitudes in the northern hemisphere based on MCS observations. MCD FFT for these cases also reveals the presence of both SPW1 ($n = 0$, $k = 1$) and SPW2 ($n = 0$, $k = 2$) in the middle atmosphere but with relatively smaller amplitudes (See Figures S2 and S3 in Supporting Information S1). Forbes et al. (2020) showed that SPWs are highly variable with L_s, which is broadly consistent with our results at high northern latitudes from observations at a fixed location.

In the upper atmosphere, for Cases 2A and 2B, MCD FFT shows that SE1 is strongest, but there is a significant presence of T0 as well. The results for Cases 2A and 2B need to be interpreted with caution due to the smaller number of data points resulting from the exclusion of days with high solar EUV. For Cases 3A and 3B, MCD FFT also shows that the S0 tide which gives rise to a wavenumber-2 structure is the largest, followed by T0, D0 and SE1(See Figures S4 and S5 in Supporting Information S1). Since observations of Case 3A suggest wavenumber-3 is dominant, disagreement with MCD is likely due to the presence of the SE1 and T0 tides, which give rise to a wavenumber-3 structure when sampled at local times they are in phase.

The relative significance of the terdiurnal tides varies among the different cases considered. The T0 tide is prominent in cases 3A and 3B at all altitudes, especially in the upper atmosphere. T0 is also prominent at upper atmospheric altitudes in cases 2A and 2B. Forbes et al. (2021) noted the presence of the zonally symmetric T0 tide in the MCD at high latitude summer hemisphere, contributing to the wavenumber-3 signature observed in the TGO aerobraking density. The T0 tide could be produced through the nonlinear interaction between DE2 and SW2 or D0 and S0 tides (Forbes et al., 2021). MCD FFT for Cases 3A and 3B indicate the presence of S0 and D0, clearly suggesting that the generation of T0 from these tides is likely in these cases. For Cases 2A and 2B, while S0 is clearly present, D0 and DE2 are also present, although the latter has a very small amplitude. While either interaction is possible, it seems more likely that S0 and D0 lead to the generation of T0 in these cases considered here as well.

4.8. Comparison to Low Latitude

The tidal perturbations in the upper atmosphere at high northern latitudes seem to be dominated by a mix of wavenumber-2 and -3 components, although wavenumber-1 and -4 components may be present in some cases. These wavenumber signatures are also present in the upper atmospheric observations at low latitudes; however, the tides responsible for producing these longitudinal variations differ from those at low latitudes. It is clear from the observations of the middle atmosphere that the semidiurnal tide is strongest, and this is in contrast with low latitudes where the diurnal tide is consistently strongest, as noted by Kumar et al. (2022). MCS observations suggest that the major contributors are likely the SE1 and DE2 tides, although some DE1, S0, SPW2, and TW1 may be present. This is in contrast with low latitudes, where the DE1 tide is identified as a major contributor to the north of the equator and the DE2 tide to the south of the equator (Kumar et al. (2022)). Furthermore, middle atmospheric observations at high latitudes suggest the presence of terdiurnal tides, which were not identified at low latitudes.

In terms of capturing the dominant wavenumber, the model exhibits less good agreement with the observations at high latitudes compared to that reported previously at lower latitudes (Kumar et al., 2022). This disparity can be attributed to the relatively comparable influence of diurnal, semidiurnal, and terdiurnal tides at high latitudes, compared to the lower latitudes where the diurnal tides play a more dominant role. Furthermore, identifying the dominant wavenumber itself is complicated when all three diurnal, semidiurnal, and terdiurnal tides are present.

Based on the comparison with observations from the middle atmosphere, the model appears to capture most of the underlying tides correctly; however, additional observations are required to more precisely constrain their amplitudes, particularly in the upper atmosphere. The amplitude of the tides in the model often compares favorably to that observed in the middle atmosphere but not in the upper atmosphere. Furthermore, the phases predicted by the model often do not align with the observations. The prediction of phases presents a challenge, especially when compared with observations at a single local time.

5. Conclusions

This study utilizes concurrent observations from the EUVM and MCS instruments on board the MAVEN and MRO spacecraft and model output from MCD to investigate the tides that reach the high latitude upper atmosphere. Focused on six cases at high northern latitudes, the dominant signatures identified are the wavenumbers-2 and -3 components. Although the dominant wavenumbers are similar to those observed at low latitudes, the underlying tides contributing to the wave structure are different. While there is a clear dominance of the diurnal tides at the low latitudes, the high northern latitudes see comparable importance among the diurnal, semidiurnal and terdiurnal tides.

An important and notable result from this study is that the dominant wavenumber can be misleading when only a single local time is considered. Furthermore, even with two sampled local times, it remains challenging to accurately identify terdiurnal components, which could be important at the higher latitudes considered in this study. Therefore, obtaining a wider range of observations with improved local time sampling of the Martian atmosphere is imperative, particularly in the high latitude regions.

Non-migrating tides can account for much of the longitudinal variability at the high northern latitudes, although stationary planetary waves may also be present. From the observations alone, the middle atmosphere seems to be dominated by the wavenumber-3 component in 4 out of 6 cases. In all these cases, the semidiurnal component is stronger than the diurnal component, revealing that the SE1 tide is the origin of the wavenumber-3 signature. While the model also sees SE1 as the strongest contributor, diurnal tides DE1 and DE2 and terdiurnal tides T0 and TW1 are also present. In the upper atmosphere, observations indicate a strong wavenumber-2 component in half of the cases, with two of the remaining cases dominated by the wavenumber-3 component and one case by the wavenumber-1 component. Model results in the upper atmosphere suggest that the contributions from the diurnal components are very small and that the semidiurnal and terdiurnal components begin to take prominence.

The model suggests that the diurnal tides, which have a strong presence in the middle atmosphere, diminish significantly as they ascend into the upper atmosphere. This indicates that the vertical propagation of the diurnal tides may be inhibited at high northern latitudes and is likely related to the zonal mean winds in this region. However, despite the model's predictions, there are no wind measurements in this region to corroborate these findings. In general, the high northern latitudes seem more variable, and more observations are required to

determine and distinguish the characteristics of the tides, particularly the terdiurnal tides and stationary planetary waves.

Appendix A: Deducing Tidal Amplitudes and Phases by Fitting to MCS Data at All Available Locations

MCS observations are typically measured "in-track" where the forward limb is viewed in the direction of the spacecraft motion. Since the MRO spacecraft is in a sun-synchronous orbit, this would also mean that the observations are locked in near two local times that are roughly ∼12 hr apart at low and mid-latitudes. The method outlined in Section 3.2 uses this difference in local time to good advantage, allowing for the separation of the diurnal tides from the semidiurnal tides. One major caveat while using this method is that the stationary planetary waves may be aliased with the semidiurnal tide and other higher-order tides. Kleinböhl et al. (2013) utilized measurements obtained from observation campaigns that covered additional local times to analyze semidiurnal tides. These observations were made by viewing the limb 90° to the left and the right with respect to the spacecraft's motion and are called "cross-track" measurements or by viewing the limb anywhere between 0 and 90°, referred to as "off-track" measurements. The resulting observations provide additional local time coverage ranging between six local times at low to mid-latitudes and seven or eight local times at high latitudes.

For Case 1A analyzed here, the additional MCS local times sampled shown in Figure A1 indicate that there are ∼8 local times between 55 and 65°N. The data selected from these local times are binned in a longitude-local time grid of 30° by 0.5 hr. This data is then averaged and the corresponding temperature field is shown in Figure A2a. The first control case is an idealized sum of the S0 and SE1 tides generated at the same locations as the MCS sampling and is shown in Figure A2b. The selection of tides to generate the simulated data is informed by the results of the analysis of MCS local time sum and difference temperatures described in Section 3.2. A model that describes the sum of the S0 and SE1 is fitted to the simulated data. The fit parameters (i.e., the amplitudes and phases of each tide) are used to reconstruct data at all longitudes and local times, as shown in Figure A2c. The derived amplitudes and phases for the S0 and SE1 tides are within 5%–10% of the simulated amplitudes and phases, as shown in Table A1.

Another fit is performed on the same simulated data but with a fit model that includes the DE1 tide in addition to the S0 and SE1 tides. Since the simulated data do not consist of the DE1 tide, the amplitude and phases associated with it are expected to be zero. As seen in Tables A1 and A2, the DE1 amplitude is nearly zero but a phase is associated with it. Since the amplitude of DE1 is zero, the resulting phase can be neglected.

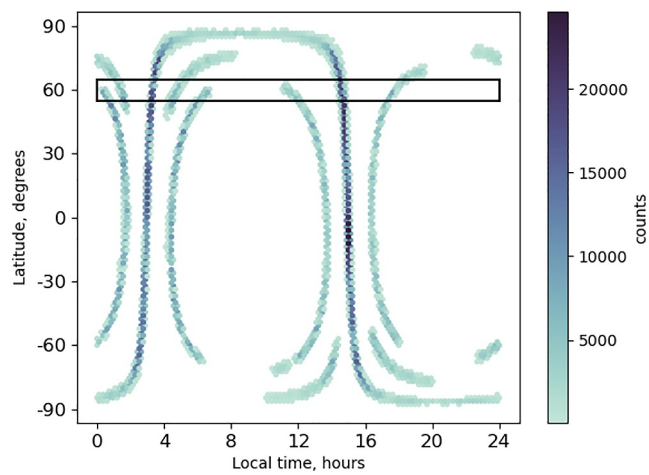

Figure A1. The MCS data distribution for Case 1A as a function of local time and longitude. The colors indicate the density of points at a particular location. The black box shows the data selected between 55 and 65°N and at all available local times.

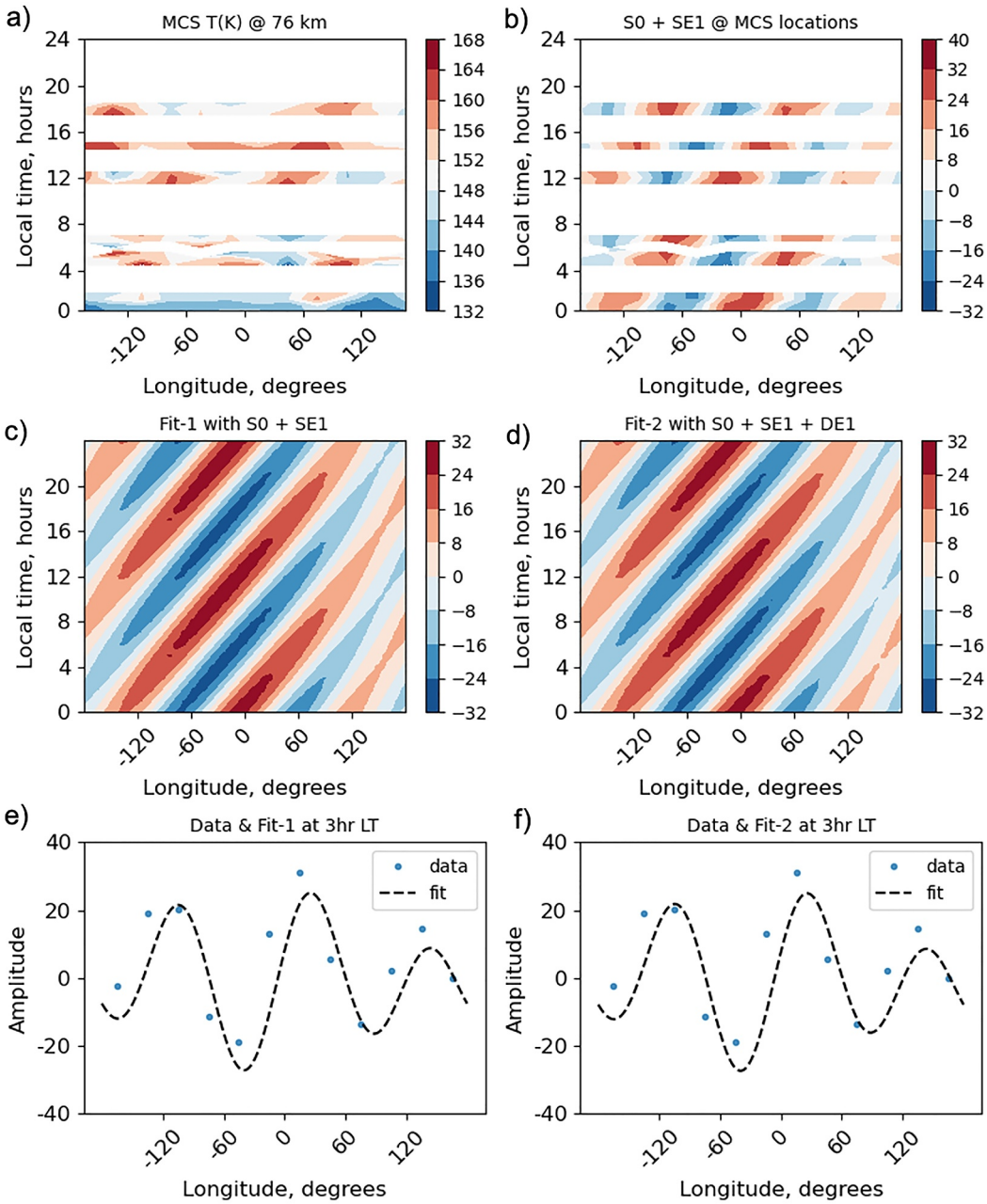

Figure A2. (a) All available MCS derived temperatures binned and averaged and shown as a function of longitude and local time for Case 1A at 76 km. The data are first binned in a longitude-local time grid of 30° × 0.5 hr and then averaged. (b) Simulated tidal field consisting of S0 and SE1 tides are generated at the same locations as the MCS data. (c) Shows the reconstruction of the tidal field by fitting to the simulated tidal field in (b) with a model assuming S0 and SE1. (d) Same as panel (c) but the model assumes S0, SE1 and DE1. (e) A slice of the reconstruction shown in (e) at 3 hr LT. (f) Same as panel (e) but for (d).

Table A1
Amplitudes of the Simulated Data Compared With a Fit Using a Model Assuming S0 and SE1

Amplitudes	S0	SE1	DE1
Original (S0 + SE1)	10	20	NA
Fitted (S0 + SE1)	9.5	17.9	
Fitted (S0 + SE1 + DE1)	9.48	17.9	0.35

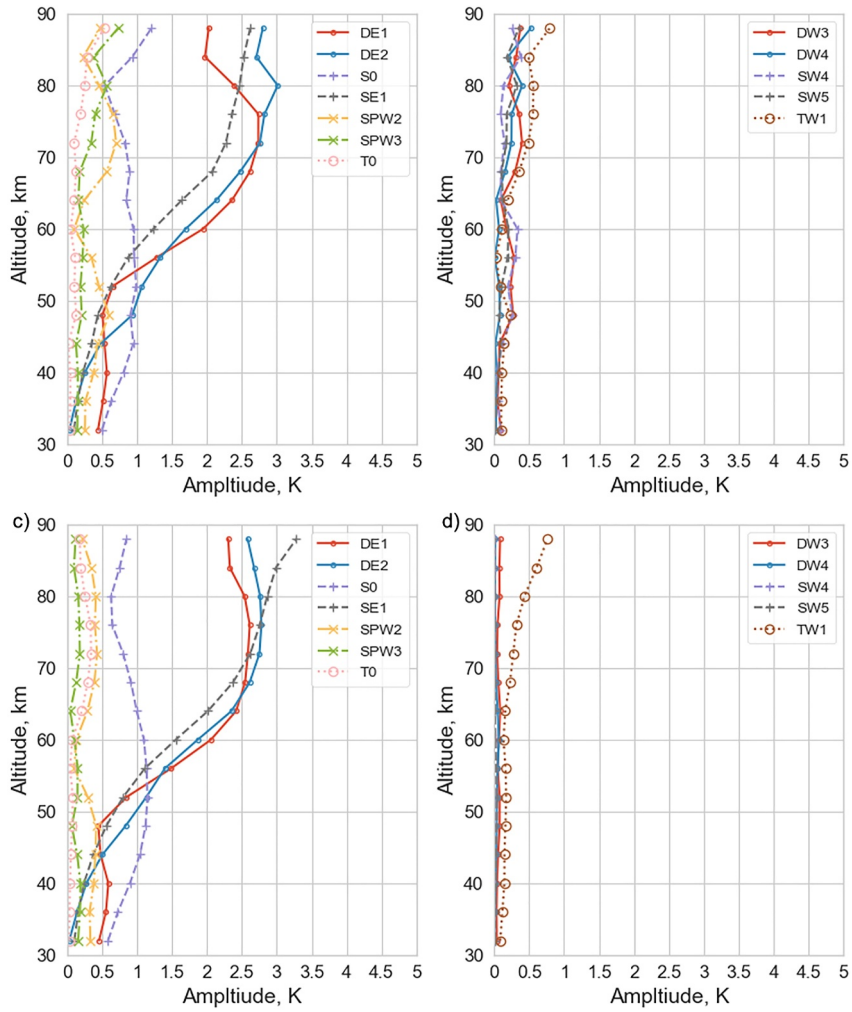

Figure A3. Compares the fit to the model sampled at the locations of the MCS observations and the Fourier decomposition using the full diurnal cycle of the model. Panels (a, b) show the amplitude as a function of altitude from fitting MCD sampled at MCS observations at all available local times between 55 and 65°N (Case 1A) for the eastward propagating DE1, DE2, SE1, TW1, T0 tides, the zonally symmetric tide S0 and the westward propagating DW3, DW4, SW4, SW5 tides. Panels (c, d) are the amplitudes of the tides obtained from the Fourier decomposition using the entire diurnal cycle representing the temperatures at all longitudes and local times for Case 1A.

To test whether this method is able to distinguish between eastward and westward propagating tides that give rise to the same zonal variation, we apply the same steps outlined above to a second test case consisting of a simulated field that includes the S0, SE1, and SW4 tides. Both the eastward propagating SE1 and westward

Table A2
Phases of the Simulated Data Compared With a Fit Using a Model Assuming S0 and SE1 and a Model Assuming S0, SE1, and DE1

Phases	S0	SE1	DE1
Original (S0 + SE1)	0	25	NA
Fitted (S0 + SE1)	1.22	25.60	
Fitted (S0 + SE1 + DE1)	1.35	25.61	72

Table A3
Amplitudes of the Simulated Data Compared With a Fit Using a Model Assuming S0 and SE1, Fit With a Model Assuming S0, SE1, and SW4, and Lastly, a Model Assuming S0, SE1, SW4, and DE1

Amplitudes	S0	SE1	SW4	DE1
Original (S0 + SE1 + SW4)	10	20	6	NA
Fitted (S0 + SE1)	10.8	17.9		
Fitted (S0 + SE1 + SW4)	9.5	17.8	5.6	
Fitted (S0 + SE1 + SW4 + DE1)	9.5	17.8	5.6	0.28

propagating SW4 tides can contribute to the wavenumber-2 structure in a fixed local time reference frame. The results from the fits to the simulated data are shown in Tables A3 and A4. It is seen that both amplitudes and phases are within 5%–10% of the expected values. Similar to the first test case, when fitting with the DE1 tide in addition to the other tides, the amplitude is nearly zero, but a phase associated with it which can be neglected.

A third test case with simulated data, which includes the terdiurnal tide TW1 along with S0, SE1 and SW5 tides, is analyzed to evaluate the method's ability to capture the terdiurnal tide. The amplitude and phase of TW1 are within 6% of the expected values as seen in Tables A5 and A6. While the method seems to perform reasonably well on the simulated data in the three test cases, a comparison is made between amplitudes derived from the MCD temperatures sampled at all available MCS locations and those obtained from an FFT performed on the entire diurnal cycle of MCD for Case 1A to establish a degree of uncertainty in the fitted amplitudes which is shown in Figure A3.

The eastward and westward propagating tides DE1, DE2, SE1, DW4, DW5, SW4, SW5, TW1, the zonally symmetric tides S0 and T0 and the stationary planetary waves SPW2 and SPW3 are fit to the MCD data. The amplitudes derived from the fit for each tide are shown as a function of altitude in Figures A3a and A3b. These amplitudes are compared to those obtained from the FFT shown in Figures A3c and A3d, and at 76 km, the amplitude of SPW2 seems to be overestimated by ∼1K and of SE1 underestimated by ∼0.5K which are the absolute errors. The absolute errors on the amplitudes of all other tides range between 0.08–0.4 K. Therefore, at 76 km in the MCD output, the tides that have the most significant amplitudes are DE2, SE1, DE1, and S0 in the order of descending amplitudes. Some TW1 and SPW2 may also be present, but these must be interpreted with caution since, in the model, these exist in very small amplitude at this altitude. A detailed discussion regarding the model and observation comparison can be found in Section 3.2.

Table A4
Phases of the Simulated Data Compared With a Fit Using a Model Assuming S0 and SE1, Fit With a Model Assuming S0, SE1, and SW4 and Lastly, a Model Assuming S0, SE1, SW4, and DE1

Phases	S0	SE1	SW4	DE1
Original (S0 + SE1 + SW4)	0	25	62	NA
Fitted (S0 + SE1)	−8.5	25.5		
Fitted (S0 + SE1 + SW4)	0.8	25.6	61.3	
Fitted (S0 + SE1 + SW4 + DE1)	0.9	25.6	61.2	71.9

Table A5
Amplitudes of the Simulated Data Compared With a Fit Using a Model Assuming S0 and SE1, Fit With a Model Assuming S0, SE1, and SW5 and Lastly, a Model Assuming S0, SE1, SW5, TW1, and DE1

Amplitudes	S0	SE1	SW5	TW1	DE1
Original (S0 + SE1 + SW5 + TW1)	10	20	6	3	NA
Fitted (S0 + SE1)	9.9	18.4			
Fitted (S0 + SE1 + SW5)	9.9	17.9	5.1		
Fitted (S0 + SE1 + SW5 + TW1 + DE1)	9.5	17.9	5.1	2.8	0.3

Table A6
Phases of the Simulated Data Compared With a Fit Using a Model Assuming S0 and SE1, Fit With a Model Assuming S0, SE1, and SW5 and Lastly, a Model Assuming S0, SE1, SW5, TW1, and DE1

Phases	S0	SE1	SW5	TW1	DE1
Original (S0 + SE1 + SW5 + TW1)	0	25	62	110	NA
Fitted (S0 + SE1)	2.1	19.5			
Fitted (S0 + SE1 + SW5 + TW1)	2.1	25	58		
Fitted (S0 + SE1 + SW5 + TW1 + DE1)	1.15	25	58	110.9	71.9

Data Availability Statement

The MAVEN EUV solar irradiance data are publicly available on the Planetary Plasma Interactions (PPI) node of NASA's Planetary Data System (Eparvier, 2023). The MAVEN mission has been funded by NASA through the Mars Exploration Program. The MCS derived data records (DDR) version 5 are publicly available from NASA's Planetary Data System (McCleese (2008)). The Mars Climate Database (MCD) version 6.1 and related software are publicly available at http://www-mars.lmd.jussieu.fr (Forget et al., 1999; Millour et al., 2017). The data products associated with this manuscript are derived from the data sets cited above and are archived in the Virginia Tech data repository that is in accordance with AGU's FAIR data policy (Kumar, 2023).

Acknowledgments
This work was supported through NASA Grant 80NSSC20K1050.

References

Angelats i Coll, M., Forget, F., López-Valverde, M. A., Read, P. L., & Lewis, S. R. (2004). Upper atmosphere of Mars up to 120 km: Mars Global Surveyor accelerometer data analysis with the LMD general circulation model. *Journal of Geophysical Research*, *109*(E1), E01011. https://doi.org/10.1029/2003JE002163

Banfield, D., Conrath, B., Pearl, J. C., Smith, M. D., & Christensen, P. (2000). Thermal tides and stationary waves on Mars as revealed by Mars Global Surveyor thermal emission spectrometer. *Journal of Geophysical Research*, *105*(E4), 9521–9537. https://doi.org/10.1029/1999JE001161

Banfield, D., Conrath, B. J., Smith, M. D., Christensen, P. R., & Wilson, R. J. (2003). Forced waves in the Martian atmosphere from MGS TES nadir data. *Icarus*, *161*(2), 319–345. https://doi.org/10.1016/S0019-1035(02)00044-1

Bell, J. M., Bougher, S. W., & Murphy, J. R. (2007). Vertical dust mixing and the interannual variations in the Mars thermosphere. *Journal of Geophysical Research*, *112*(E12), E12002. https://doi.org/10.1029/2006JE002856

Bougher, S. W., Engel, S., Hinson, D. P., & Forbes, J. M. (2001). Mars Global Surveyor radio science electron density profiles: Neutral atmosphere implications. *Geophysical Research Letters*, *28*(16), 3091–3094. https://doi.org/10.1029/2001GL012884

Cahoy, K. L., Hinson, D. P., & Tyler, G. L. (2007). Characterization of a semidiurnal eastward-propagating tide at high northern latitudes with Mars Global Surveyor electron density profiles. *Geophysical Research Letters*, *34*(15), L15201. https://doi.org/10.1029/2007GL030449

Conrath, B. J. (1976). Influence of planetary-scale topography on the diurnal thermal tide during the 1971 Martian dust storm. *Journal of the Atmospheric Sciences*, *33*, 24115.

Ekanayake, E. M. P., Aso, T., & Miyahara, S. (1997). Background wind effect on propagation of nonmigrating diurnal tides in the middle atmosphere. *Journal of Atmospheric and Solar-Terrestrial Physics*, *59*(4), 401–429. https://doi.org/10.1016/S1364-6826(96)00012-0

England, S. L., Jain, S., Deighan, J., Chaffin, M. S., Holsclaw, G., Evans, J. S., et al. (2022). Spatial structure of far ultraviolet Martian dayglow observed by EMM-EMUS. https://doi.org/10.1002/essoar.10511549.1

England, S. L., Liu, G., Kumar, A., Mahaffy, P. R., Elrod, M., Benna, M., et al. (2019). Atmospheric tides at high latitudes in the Martian upper atmosphere observed by MAVEN and MRO. *Journal of Geophysical Research: Space Physics*, *124*(4), 2943–2953. https://doi.org/10.1029/2019JA026601

England, S. L., Liu, G., Withers, P., Yiğit, E., Lo, D., Jain, S., et al. (2016). Simultaneous observations of atmospheric tides from combined in situ and remote observations at Mars from the MAVEN spacecraft. *Journal of Geophysical Research: Planets*, *121*(4), 594–607. https://doi.org/10.1002/2016JE004997

Eparvier, F. G. (2023). MAVEN EUV modelled data bundle [Dataset]. *NASA Planetary Data System*. https://doi.org/10.17189/1517691

Eparvier, F. G., Chamberlin, P. C., Woods, T. N., & Thiemann, E. M. B. (2015). The solar extreme ultraviolet monitor for MAVEN. *Space Science Reviews*, *195*(1–4), 293–301. https://doi.org/10.1007/s11214-015-0195-2

Fan, S., Forget, F., Smith, M. D., Guerlet, S., Badri, K. M., Atwood, S. A., et al. (2022). Migrating thermal tides in the Martian atmosphere during aphelion season observed by EMM/EMIRS. *Geophysical Research Letters*, *49*(18), e2022GL099494. https://doi.org/10.1029/2022GL099494

Fan, S., Guerlet, S., Forget, F., Bierjon, A., Millour, E., Ignatiev, N., et al. (2022). Thermal tides in the Martian atmosphere near northern summer solstice observed by ACS/TIRVIM onboard TGO. *Geophysical Research Letters*, *49*(7), e2021GL097130. https://doi.org/10.1029/2021GL097130

Forbes, J. M., Bridger, A. F. C., Bougher, S. W., Hagan, M. E., Hollingsworth, J. L., Keating, G. M., & Murphy, J. (2002). Nonmigrating tides in the thermosphere of Mars. *Journal of Geophysical Research*, *107*(E11), 23-1–23-12. https://doi.org/10.1029/2001JE001582

Forbes, J. M., Bruinsma, S., Zhang, X., Forget, F., Marty, J., Millour, E., & González-Galindo, F. (2021). The wave origins of longitudinal structures in ExoMars Trace Gas Orbiter (TGO) aerobraking densities. *Journal of Geophysical Research: Space Physics*, *126*(2), e2020JA028769. https://doi.org/10.1029/2020JA028769

Forbes, J. M., & Hagan, M. E. (2000). Diurnal Kelvin wave in the atmosphere of Mars: Towards an understanding of "stationary" density structures observed by the MGS accelerometer. *Geophysical Research Letters*, *27*(21), 3563–3566. https://doi.org/10.1029/2000GL011850

Forbes, J. M., Hagan, M. E., Bougher, S. W., & Hollingsworth, J. L. (2001). Kelvin wave propagation in the upper atmospheres of Mars and Earth. *Advances in Space Research*, *27*(11), 1791–1800. https://doi.org/10.1016/S0273-1177(01)00286-1

Forbes, J. M., Zhang, X., Fang, X., Benna, M., González-Galindo, F., Forget, F., & Millour, E. (2023). Solar-synchronous tides in Mars thermosphere CO_2, Ar, and N_2 densities from MAVEN. *Journal of Geophysical Research: Space Physics*, *128*(8), e2023JA031637. https://doi.org/10.1029/2023JA031637

Forbes, J. M., Zhang, X., Forget, F., Millour, E., & Kleinböhl, A. (2020). Solar tides in the middle and upper atmosphere of Mars. *Journal of Geophysical Research: Space Physics*, *125*(9). https://doi.org/10.1029/2020JA028140

Forget, F., Hourdin, F., Fournier, R., Hourdin, C., Talagrand, O., Collins, M., et al. (1999). Improved general circulation models of the Martian atmosphere from the surface to above 80 km. *Journal of Geophysical Research*, *104*(E10), 24155–24175. https://doi.org/10.1029/1999JE001025

Guerlet, S., Fan, S., Forget, F., Ignatiev, N., Millour, E., Kleinböhl, A., et al. (2023). Thermal tides on mars before and during the 2018 global dust event as observed by TIRVIM-ACS onboard ExoMars trace gas orbiter. *Journal of Geophysical Research: Planets*, *128*(9), e2023JE007851. https://doi.org/10.1029/2023JE007851

Guzewich, S. D., Talaat, E. R., & Waugh, D. W. (2012). Observations of planetary waves and nonmigrating tides by the Mars Climate Sounder. *Journal of Geophysical Research*, *117*(E3), E03010. https://doi.org/10.1029/2011JE003924

Jones, M., Forbes, J. M., & Sassi, F. (2019). The effects of vertically propagating tides on the mean dynamical structure of the lower thermosphere. *Journal of Geophysical Research: Space Physics*, *124*(8), 7202–7219. https://doi.org/10.1029/2019JA026934

Keating, G. M., Bougher, S. W., Zurek, R. W., Tolson, R. H., Cancro, G. J., Noll, S. N., et al. (1998). The structure of the upper atmosphere of Mars: In situ accelerometer measurements from Mars Global Surveyor. *Science*, *279*(5357), 1672–1676. https://doi.org/10.1126/science.279.5357.1672

Kleinböhl, A., John Wilson, R., Kass, D., Schofield, J. T., & McCleese, D. J. (2013). The semidiurnal tide in the middle atmosphere of Mars. *Geophysical Research Letters*, *40*(10), 1952–1959. https://doi.org/10.1002/grl.50497

Kleinböhl, A., Schofield, J. T., Kass, D. M., Abdou, W. A., Backus, C. R., Sen, B., et al. (2009). Mars Climate Sounder limb profile retrieval of atmospheric temperature, pressure, and dust and water ice opacity. *Journal of Geophysical Research*, *114*(E10), E10006. https://doi.org/10.1029/2009JE003358

Kumar, A. (2023). Data associated with "atmospheric tides in the middle and upper atmosphere of Mars at northern high latitudes: A comparison of MAVEN-EUVM and MRO-MCS observations with model results" (p. 68679514 bytes). [Dataset]. *University Libraries, Virginia Tech*. https://doi.org/10.7294/22659343

Kumar, A., England, S. L., Liu, G., Jain, S., & Schneider, N. M. (2022). Observations of atmospheric tides in the middle and upper atmosphere of Mars from MAVEN and MRO. *Journal of Geophysical Research: Planets*, *127*(8), e2022JE007290. https://doi.org/10.1029/2022JE007290

Lee, C., Lawson, W. G., Richardson, M. I., Heavens, N. G., Kleinböhl, A., Banfield, D., et al. (2009). Thermal tides in the Martian middle atmosphere as seen by the Mars climate sounder. *Journal of Geophysical Research*, *114*(E3), E03005. https://doi.org/10.1029/2008JE003285

Liu, G., England, S., Lillis, R. J., Mahaffy, P. R., Elrod, M., Benna, M., & Jakosky, B. (2017). Longitudinal structures in Mars' upper atmosphere as observed by MAVEN/NGIMS: Upper atmosphere longitudinal structures. *Journal of Geophysical Research: Space Physics*, *122*(1), 1258–1268. https://doi.org/10.1002/2016JA023455

Lo, D. Y., Yelle, R. V., Schneider, N. M., Jain, S. K., Stewart, A. I. F., England, S. L., et al. (2015). Nonmigrating tides in the Martian atmosphere as observed by MAVEN IUVS. *Geophysical Research Letters*, *42*(21), 9057–9063. https://doi.org/10.1002/2015GL066268

Mazarico, E., Zuber, M. T., Lemoine, F. G., & Smith, D. E. (2008). Observation of atmospheric tides in the Martian exosphere using Mars Reconnaissance Orbiter radio tracking data. *Geophysical Research Letters*, *35*(9), L09202. https://doi.org/10.1029/2008GL033388

McCleese, D. J. (2008). *MRO mars climate sounder derived data records V1.0*. NASA Planetary Data System. https://doi.org/10.17189/P73K-XY37

McCleese, D. J., Schofield, J. T., Taylor, F. W., Calcutt, S. B., Foote, M. C., Kass, D. M., et al. (2007). Mars climate sounder: An investigation of thermal and water vapor structure, dust and condensate distributions in the atmosphere, and energy balance of the polar regions. *Journal of Geophysical Research*, *112*(E5), E05S06. https://doi.org/10.1029/2006JE002790

Millour, E., Forget, F., Spiga, A., Vals, M., Zakharov, V., Navarro, T., et al., & MCD/GCM Development Team. (2017). The Mars climate database (MCD version 5.3). 12247.

Moudden, Y., & Forbes, J. M. (2008). Effects of vertically propagating thermal tides on the mean structure and dynamics of Mars' lower thermosphere. *Geophysical Research Letters*, *35*(23), L23805. https://doi.org/10.1029/2008GL036086

Schneider, N. M., Milby, Z., Jain, S. K., González-Galindo, F., Royer, E., Gérard, J.-C., et al. (2020). Imaging of Martian circulation patterns and atmospheric tides through MAVEN/IUVS nightglow observations. *Journal of Geophysical Research: Space Physics*, *125*(8), e2019JA027318. https://doi.org/10.1029/2019JA027318

Steele, L. J., Kleinböhl, A., Kass, D. M., & Zurek, R. W. (2021). Aerosols and tides in the Martian tropics during Southern Hemisphere spring equinox from Mars climate sounder data. *Journal of Geophysical Research: Planets*, *126*(4), e2020JE006776. https://doi.org/10.1029/2020JE006776

Teitelbaum, H., & Vial, F. (1991). On tidal variability induced by nonlinear interaction with planetary waves. *Journal of Geophysical Research*, *96*(A8), 14169–14178. https://doi.org/10.1029/91JA01019

Thaller, S. A., Andersson, L., Pilinski, M. D., Thiemann, E., Withers, P., Elrod, M., et al. (2020). Tidal wave-driven variability in the Mars ionosphere-thermosphere system. *Atmosphere*, *11*(5), 521. https://doi.org/10.3390/atmos11050521

Thiemann, E. M. B., Eparvier, F. G., Bougher, S. W., Dominique, M., Andersson, L., Girazian, Z., et al. (2018). Mars thermospheric variability revealed by MAVEN EUVM solar occultations: Structure at aphelion and perihelion and response to EUV forcing. *Journal of Geophysical Research: Planets*, *123*(9), 2248–2269. https://doi.org/10.1029/2018JE005550

Wilson, R. J. (1997). A general circulation model simulation of the Martian polar warming. *Geophysical Research Letters*, *24*(2), 123–126. https://doi.org/10.1029/96GL03814

Wilson, R. J. (2000). Evidence for diurnal period Kelvin waves in the Martian atmosphere from Mars Global Surveyor TES data. *Geophysical Research Letters*, *27*(23), 3889–3892. https://doi.org/10.1029/2000GL012028

Wilson, R. J. (2002). Evidence for nonmigrating thermal tides in the Mars upper atmosphere from the Mars Global Surveyor accelerometer experiment. *Geophysical Research Letters*, *29*(7), 1120. https://doi.org/10.1029/2001GL013975

Withers, P., Bougher, S. W., & Keating, G. M. (2003). The effects of topographically-controlled thermal tides in the Martian upper atmosphere as seen by the MGS accelerometer. *Icarus*, *164*(1), 14–32. https://doi.org/10.1016/S0019-1035(03)00135-0

Withers, P., & Catling, D. C. (2010). Observations of atmospheric tides on Mars at the season and latitude of the Phoenix atmospheric entry. *Geophysical Research Letters*, *37*(24), L24204. https://doi.org/10.1029/2010GL045382

Withers, P., Pratt, R., Bertaux, J.-L., & Montmessin, F. (2011). Observations of thermal tides in the middle atmosphere of Mars by the SPICAM instrument. *Journal of Geophysical Research*, *116*(E11), E11005. https://doi.org/10.1029/2011JE003847

Wu, Z., Li, T., & Dou, X. (2015). Seasonal variation of Martian middle atmosphere tides observed by the Mars Climate Sounder. *Journal of Geophysical Research: Planets*, *120*(12), 2206–2223. https://doi.org/10.1002/2015JE004922

Zurek, R. W. (1976). Diurnal tide in the Martian atmosphere. *Journal of the Atmospheric Sciences*, *33*(2), 321–337. https://doi.org/10.1175/1520-0469